



3D-PRINTED ELECTRODES FOR ENERGY STORAGE

Investigating the rheology of 2D titanium carbide (MXene) dispersions for colloidal processing: Progress and challenges

Michael Greaves¹, Mana Mende¹, Jiacheng Wang¹, Wenji Yang¹, Suelen Barg^{1,2,a)}

¹Department of Materials, Henry Royce Institute Hub Building, University of Manchester, Oxford Road, Manchester M13 9PL, UK

²Institute of Materials Resource Management (MRM), Augsburg University, Am Technologiezentrum 8, 86159 Augsburg, Germany

a) Address all correspondence to this author. e-mail: suelen.barg@mrm.uni-augsburg.de

Received: 4 May 2021; accepted: 22 June 2021; published online: 8 July 2021

Among 2D materials, MXenes (especially their most studied member, titanium carbide) present a unique opportunity for application via colloidal processing, as they are electrically conductive and chemically active, whilst still being easily dispersed in water. And since the first systematic study of colloidal MXene rheology was published in 2018 (*Rheological Characteristics of 2D Titanium Carbide (MXene) Dispersions: A Guide for Processing MXenes* by Akuzum, et al.), numerous works have presented small amounts of rheological data which together contribute to a deeper understanding of the topic. This work reviews the published rheological data on all MXene-containing formulations, including liquid crystals, mixtures and non-aqueous colloids, which have been used in processes such as stamping, patterning, 2D and 3D printing. An empirical model of aqueous titanium carbide viscosity has been developed, and recommendations are made to help researchers more effectively present their data for future rheological analysis.

Introduction

MXenes—2D transition metal carbides, nitrides and carbonitrides—present a unique opportunity for colloidal processing techniques, as they have been shown on many occasions to be hydrophilic and chemically reactive like graphene oxide (GO) without compromising on their electrical conductivity, which can match that of graphene [1–4]. Therefore, in light of its potential usefulness, the most well-understood MXene, titanium carbide ($Ti_3C_2T_x$, where T_x represents various surface termination groups that arise during synthesis—taken to be a mixture of –OH, –O and –F unless otherwise stated), has been the recipient of great research interest for many applications, including energy storage, electromagnetic interference (EMI) shielding, water purification and catalysis [5].

The presence of polar and protic terminal groups on the surface of $Ti_3C_2T_x$ layers makes it very hydrophilic and, thus, easily dispersed to create dilute colloids in a number of polar solvents [6], and at higher concentrations, an inhomogeneous arrangement of charges on the 2D monolayers (positively charged at the edges, and negatively charged on the basal plane) allows

samples to swell like clay as flakes come together to form a range of soft microstructures [7, 8]. These properties, in combination with the 2D morphology of MXene flakes, cause them to greatly influence the rheology of colloids and pastes, such that they can be used to make formulations suitable for a wide range of both novel and traditional processing techniques. Therefore, $Ti_3C_2T_x$ is capable of acting as both an effective rheological additive and a functionally active material in applications such as 3D-printed supercapacitors [9] and batteries [10].

The discovery of MXenes was only 10 years ago at the time of publishing this review, and as such, the growing interest in processing routes to MXene-containing products is a recent phenomenon, and publications on MXene-based inks and their rheological characteristics have only come about in the last few years (Fig. 1). To date, one paper by Akuzum, et al. in 2018 [11] has systematically investigated the rheological characteristics of a MXene colloid ($Ti_3C_2T_x$ in water), and as discussed below, it showed that aqueous $Ti_3C_2T_x$ is viscoelastic and shear thinning, meaning that viscosity measurements taken at a single shear rate are inadequate [11–14]. Since the publication of that study,

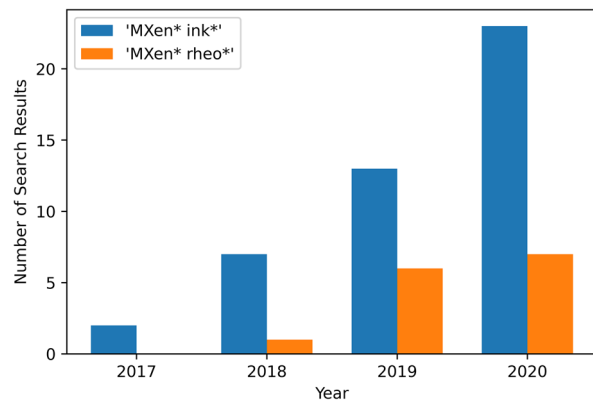


Figure 1: Number of publications returned from the Web of Science Core Collection (www.webofknowledge.com, accessed 4th January 2021) using search terms 'MXen* ink*' and 'MXen* rheo*', sorted by year.

numerous works have investigated colloidal processing routes to MXene-containing products, and they have often presented the results of rheological experiments to justify the use of MXenes in their formulations [15]. Individually, these experiments serve a limited purpose, but by bringing them together, this review aims to draw new conclusions and develop a deeper understanding of $\text{Ti}_3\text{C}_2\text{T}_x$ MXene rheology as a whole.

Review methodology

Rheological studies of MXene-based formulations were sought for through the Web of Science Core Collection (www.webofknowledge.com) using the search terms 'MXen* ink*' and 'MXen* rheo*' (where the asterisk (*) wildcard enables the search of any word that begins with the preceding characters) on 12th January 2021. All of the search results were examined, and rheological data were taken from the text, tables and plots of both main articles and their supplementary data. The open source software WebPlotDigitizer (Version 4.3, available at <https://apps.automeris.io/wpd/>) was used to extract data from plots.

Discussion

Aqueous single-layer MXene

The vast majority of 2D $\text{Ti}_3\text{C}_2\text{T}_x$ flakes in a typical dispersion prepared by the so called 'MILD' (minimally intensive layer delamination) method are single-layer, flexible, random polygons of thickness *ca.* 2 nm, and lateral diameter *ca.* 1 μm . They can, therefore, be described geometrically by their average lateral diameter, Z , as even when there are some few-layer particles in a dispersion, their lateral size far exceeds their thickness [4, 9, 16–18]. While there are many questions still left unanswered, and there are some aspects in which they remain

to be fully characterised, the apparent similarity of $\text{Ti}_3\text{C}_2\text{T}_x$ samples prepared by the MILD method allows for fruitful comparison. Here, unless stated otherwise, the phrases "single" or "mono"-layer $\text{Ti}_3\text{C}_2\text{T}_x$ shall refer to $\text{Ti}_3\text{C}_2\text{T}_x$ MXenes prepared by variations on this common method.

In 2018, Akuzum et al.[11] sought to elucidate the viscoelastic properties of both single- and multilayer MXene dispersions (multilayer dispersions are discussed in the next section). In this work, a concentric cylinder rheometer was used: aqueous dispersions of monolayer $\text{Ti}_3\text{C}_2\text{T}_x$ ($Z \approx 1 \mu\text{m}$) were placed in the small gap between two concentric cylinders, and shear force was applied to the colloid by either steady rotation of these cylinders at a range of speeds (Fig. 2a), or oscillatory rotation of the cylinders over a range of frequencies, ω , at a fixed amplitude (Fig. 2b–e). The results presented show that viscosity, η , increased with MXene concentration (as demonstrated up to 3.6 mg ml^{-1} —approximately equal to 0.4 wt% or 0.1 vol%), and decreased with increasing shear rate. That is to say, the colloids were shear thinning, and even a low concentration of MXene (0.18 mg ml^{-1}) endowed the colloid with a zero-shear viscosity of 5 mPa s ($5 \times$ that of water).

The resistance to deformation of a material that is under oscillatory shear stress can be measured by the complex modulus, G^* , which is the ratio of the stress applied and the resulting strain. Now, when under oscillatory shear stress, the deformation of elastic solids occurs simultaneously with the force applied, i.e. stress and strain are in phase with each other, and conversely, when oscillatory shear stress is applied to purely viscous materials (classical liquids), the resulting deformation occurs after a time delay—stress and strain are 90° out of phase. Therefore, the interplay between viscous and elastic behaviours in a viscoelastic material can be assessed by examining the phase difference between stress and strain, and mathematically, the complex modulus can be separated into two components: the storage modulus, G' , which measures the energy stored by a material (elastic behaviour), and the loss modulus, G'' , which measures the energy lost as heat (viscous behaviour).

$$G^* = G' + iG'' \quad (1)$$

$$G' = \frac{\sigma}{\varepsilon} \cos \delta \quad (2)$$

$$G'' = \frac{\sigma}{\varepsilon} \sin \delta \quad (3)$$

Here, σ is the stress applied, ε is the resulting strain, δ is the phase difference between stress and strain and $i = \sqrt{-1}$. To learn more about the fundamentals of viscoelasticity, which is beyond the scope of this review, we recommend the book *Understanding Viscoelasticity* by Nhan Phan-Thien,

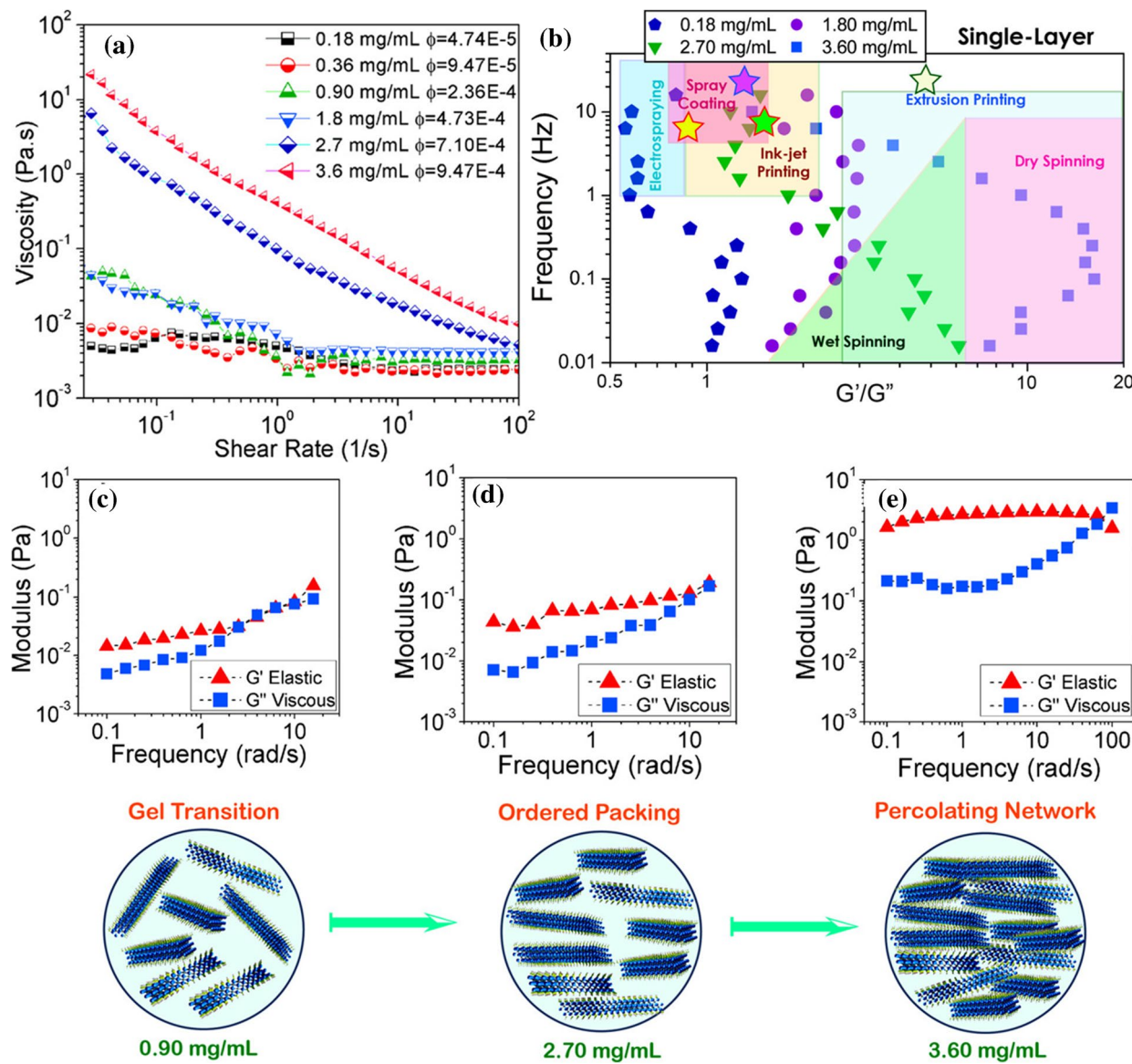


Figure 2: Viscoelastic behaviour of $0.18\text{--}3.60 \text{ mg ml}^{-1}$ (volume fraction, ϕ , $4.74 \times 10^{-5}\text{--}9.47 \times 10^{-4}$) single-layer $\text{Ti}_3\text{C}_2\text{T}_x$ in water. (a) Viscosity vs. shear rate. (b) Frequency dependency of G'/G'' and graph regions appropriate for typical fabrication processes. The stars represent the approximate parameters used in different applications of MXenes from the literature. (c–e) Frequency sweeps performed at 0.1% strain amplitude. Adapted with permission from Akuzum, et al. [11]. © 2018 American Chemical Society.

or the online seminar *Essential Tools for the New Rheologist* given by Neil Cunningham [19, 20].

Evaluating the viscoelastic moduli of aqueous $\text{Ti}_3\text{C}_2\text{T}_x$ below 0.90 mg ml^{-1} , G' was found to dominate at very low frequencies, and colloidal $\text{Ti}_3\text{C}_2\text{T}_x$ behaved as a viscoelastic soft solid, but G'' soon overtook it, and both exhibited power law scaling over the majority of the frequency range tested. Viscous-dominant fluids with a small elastic component such as these are ideal for spray coating and spin coating, because the elasticity dampens perturbations which can cause defects in purely viscous fluids, and the fact that $\text{Ti}_3\text{C}_2\text{T}_x$ exhibits this

behaviour at such low concentrations lends itself to the application of MXenes in the formation of thin films.

At 0.90 mg ml^{-1} , the relationship between moduli and oscillatory frequency began to change, indicating that a gel transition occurred about this point (Fig. 2c). Indeed, the dominance of G' ($\approx 20 \text{ mPa}$) in 0.9 mg ml^{-1} ($\phi = 2.36 \times 10^{-4}$) $\text{Ti}_3\text{C}_2\text{T}_x$ at low frequencies indicates that a solid-like, percolating network was present, and this is also evidenced by the power law relationship seen between viscosity and concentration at volume fractions above 0.90 mg ml^{-1} . The fact that percolation—the formation of a continuous 3D network throughout the entire

sample—occurred at such a low concentration indicates that the $Ti_3C_2T_x$ particles interact at very long distances via electrostatic forces (*cf.* kaolin clay [21] and polystyrene spheres [22], which effect rheology in a similar way but at $\approx 1000\times$ higher volume fraction). Although MXenes are flexible, and do not act as rigid discs [23], it is useful to consider the critical volume fraction, ϕ^* , of charged disc-shaped particles given by Jorgun and Zukoski [21]:

$$\phi^* \propto \frac{h}{d} \left(1 + \frac{2}{dk}\right)^{-3} \quad (4)$$

Here, h/d is the flake aspect ratio (thickness/diameter), and k^{-1} is the Debye screening length (*cf.* DLVO theory). Thus, the critical volume fraction, and by extension the rheology of a dispersion, will be strongly dependent on both the particles' surface charges and the electromagnetic permittivity of their surrounding medium. In practice, these factors can be easily accounted for by measuring the ζ -potential of a MXene sample. Literature values of aqueous $Ti_3C_2T_x$ ζ -potential are typically in the range -30 to -60 mV at neutral pH [8, 24], due to the high number of deoxygenated alcohol functional groups on the flake surface, and since values of this magnitude are generally considered sufficient to prevent colloid flocculation, they should also be expected to impact colloid rheology.

At higher concentrations, G' (≈ 2 Pa at 3.60 mg ml^{-1}) became independent of frequency, ω , indicating an increase in the long-range order of the percolating network, and a transition to soft gel-like behaviour (Fig. 2d, e). This is the regime in which processing techniques such as wet spinning, commonly used with weak gels, become useful.

Depending on the concentration of $Ti_3C_2T_x$ chosen, a wide range of viscosities, elastic moduli, and G'/G'' vs. ω relationships is achieved by Akuzum et al. providing theoretical support for the use of $Ti_3C_2T_x$ in processes such as spray coating, inkjet printing, and wet spinning (Fig. 2b). Indeed, painting, stamping, and pen on paper writing of aqueous MXenes were quickly achieved after their work was published [25]. However, the highest absolute value of G' measured for single-layer MXene was not sufficient for extrusion-based 3D printing.

As discussed by Corker [26] and M'Barki et al. [27], one of the key experiments in determining the suitability of a viscoelastic ink for extrusion-based 3D printing (also referred to as direct ink writing (DIW) or robocasting) is a sweep of oscillatory shear stress or strain at a fixed frequency, ω . This explores the transition from small angle oscillatory stress (the regime where there is a linear relationship between stress and strain) to large angle oscillatory stress (the regime where stress and strain have a more complex mathematical relationship), and the change in G' and G'' throughout the transition from linear to non-linear behaviour can be plotted as a function of either stress, σ , or strain, γ . Fig. 3b exemplifies this, showing a

solid-like boehmite suspension with a high storage modulus, G' , at low strain amplitude, which becomes a liquid-like suspension above the oscillatory yield strain, γ_y^{Osc} , which here is defined as the strain at which $G' = G''$ (oscillatory yield stress, σ_y^{Osc} , is defined in a similar way).

A complimentary test sweeps linear shear strain rate, $\dot{\gamma}$, imitating the forces experienced during extrusion from a reservoir, through a nozzle and onto a substrate (zero shear to high shear to zero shear). The results of this can be plotted as shear stress against strain rate (Fig. 3a) to find a static yield stress, σ_y^{Stat} , and a Herschel–Bulkley fitting can be used to find a dynamic yield stress, σ_y^{Dyn} . The static yield stress represents the force needed to initiate flow, and the dynamic yield stress represents the force needed to maintain it. Therefore, σ_y^{Stat} must be applied to an ink in order for it to start exiting the printing nozzle, and upon adhesion to the substrate, the ink must experience less than σ_y^{Dyn} in order for it to stop flowing. As oscillation frequency affects the oscillatory yield stress measured, it is good practice to perform both linear and oscillatory tests on a material to get information which is applicable to extrusion printing [27].

As a minimum requirement, robocasting demands that at rest, inks have the ability to withstand both surface tension, γ_s , and the weight of subsequently printed layers (Fig. 3c). So that structures maintain their shape with minimal strain (strain being the ratio of the applied stress and the modulus of a material), G' must be much greater than the sum of applied forces (weight and γ_s). And, since G' will significantly decrease if the total applied stress exceeds the yield stress ($\sigma > \sigma_y$), the yield stress, σ_y , must be at least comparable to this sum. This is represented by the following inequalities:

$$E_G = \frac{G'_{LVR}}{\rho gh + \gamma_s R^{-1}} \gg 1 \quad (5)$$

$$E_y = \frac{\sigma_y}{\rho gh + \gamma_s R^{-1}} \geq 1 \quad (6)$$

Here, G'_{LVR} is the storage modulus in the linear viscoelastic (low strain) region of a plot like that shown in Fig. 3b, ρ is the ink's density, h is the printed product's height, g is gravitational acceleration and R is the diameter of a printed filament (approximately that of the extrusion nozzle) [27].

How great the yield stress needs to be also depends on how abrupt the transition between linear and non-linear viscoelastic behaviour is. Short of providing a graph like that in Fig. 3b, this transition can be described using the flow transition index (FTI), which is the ratio of the oscillatory yield stress, σ_y^{Osc} , to the oscillatory stress at which G' is equal to 90% of G'_{LVR} [26]. Thus, FTI measures the length of the transition or 'yield zone', and inks with a smaller yield zone will have a smaller value of FTI. If the FTI is small, then the yield zone can be more reasonably represented by a single value, and σ_y^{Osc} can be substituted for σ_y .

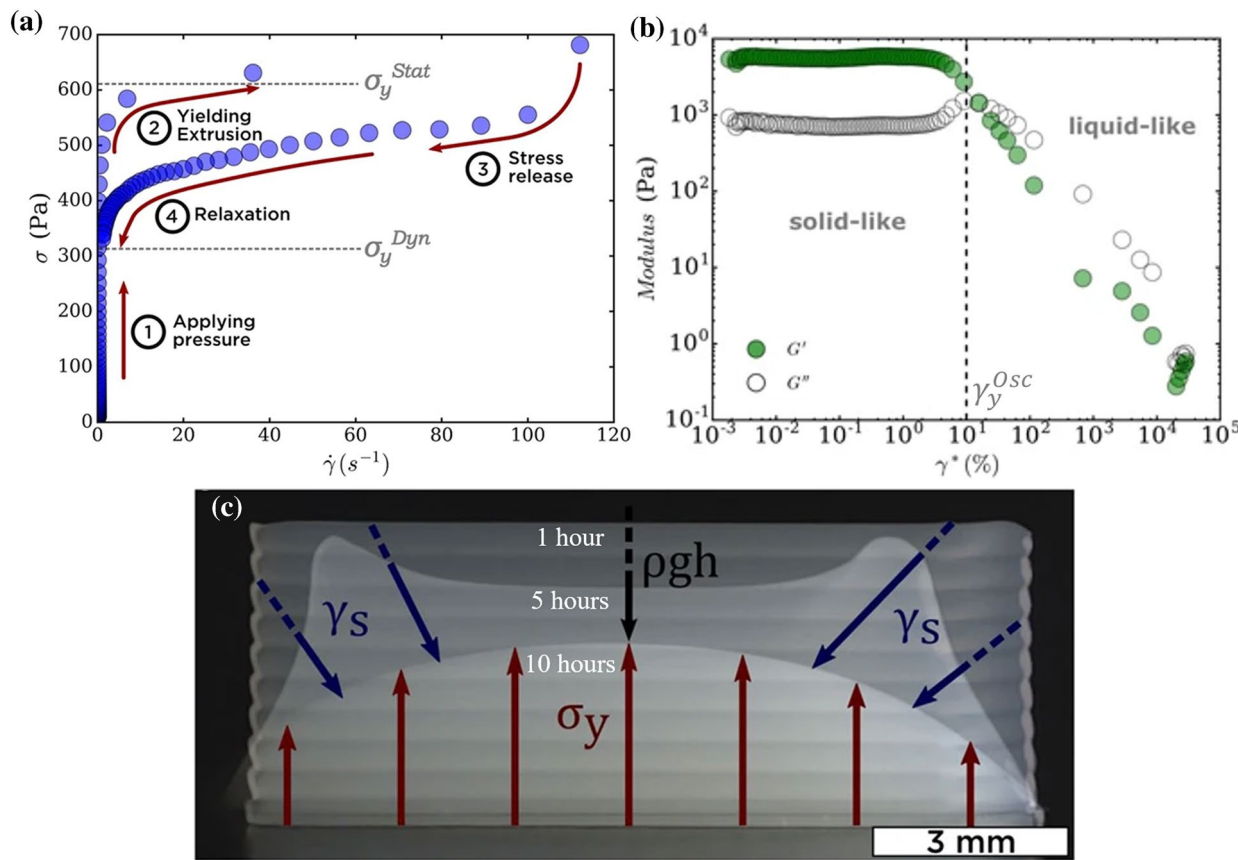


Figure 3: Behaviour of a 45 wt% boehmite aqueous suspension. (a) Loop flow curve of shear stress vs. shear strain rate. This protocol replicates the shear forces experienced during extrusion from a syringe onto a substrate and obtains values for static, σ_y^{Stat} and dynamic yield stresses, σ_y^{Dyn} . (b) Elastic, G' , and viscous, G'' , moduli vs. oscillatory strain obtained by amplitude sweep at 1 Hz. It is shown that $G' > G''$ up to the oscillatory yield strain, γ_y^{osc} , beyond which $G'' > G'$, indicating a transition from predominantly solid- to predominantly liquid-like behaviour. **c** Frame superposition of a suspension 1 h, 5 h and 10 h after printing with a 500 μm nozzle. Yield stress, σ_y , must withstand both surface tension, γ_s , and structure weight, pgh , to avoid deformation. Adapted from M'Barki et al. [27] under a Creative Commons Attribution 4.0 International Licence.

to achieve a practical value of Ξ_y . If the FTI is large this is not appropriate, and a lower value should be used for σ_y in Eq. (6). Tabulated values of $pgh + \gamma_s R^{-1}$ (Table 1) reveal that researchers looking to print new materials using robocasting should formulate inks with a resting storage modulus, G'_{LVR} , of at least 10^4 - 10^5 Pa, and a yield stress, σ_y , of at least a few hundred pascals. These demands increase substantially for structures taller than *ca.* 5 cm and filament diameters as small as 50 μm . It can also be seen that while product weight is the most important factor to consider in most cases, capillary forces begin to dominate when small structures are printed with fine needles, such as when 3D printing is used to achieve device miniaturisation.

In general, when the concentration of aqueous, monolayer $\text{Ti}_3\text{C}_2\text{T}_x$ is low ($< 10 \text{ mg ml}^{-1}$), G' and σ_y do not meet the calculated requirements of extrusion printing. However, increasing the concentration far beyond the point of percolation does not produce floccs, but rather causes the formation of a nematic liquid crystal phase [17]. Therefore, multiple papers have been able to show that at high enough concentrations, additive-free,

TABLE 1: Example values of σ_y/Ξ_y , assuming the surface tension of an ink, γ_s , is comparable to pure water (72 mN m^{-1}) [27, 28].

$\rho/\text{g ml}^{-1}$	h/cm	$R/\mu\text{m}$	$(pgh + \gamma_s R^{-1})/\text{Pa}$	$pgh/\gamma_s R^{-1}$
1.0	0.5	50	1489	0.03
2.0	0.5	50	1538	0.07
1.0	0.5	200	409	0.14
2.0	0.5	200	458	0.27
1.0	1.0	500	242	0.68
1.0	1.0	1000	170	1.36
2.0	1.0	500	340	1.36
2.0	1.0	1000	268	2.73
1.0	5.0	50	1931	0.34
2.0	5.0	50	2421	0.68
1.0	5.0	500	635	3.41
1.0	5.0	1000	563	6.81
2.0	5.0	500	1125	6.81
2.0	5.0	1000	1053	13.63

aqueous, monolayer $\text{Ti}_3\text{C}_2\text{T}_x$ is able to form 3D structures via DIW [9, 10, 29].

First, Yang et al. developed additive-free water-based inks using large (lateral size, $Z = 8.0 \pm 2.7 \mu\text{m}$), monolayer $\text{Ti}_3\text{C}_2\text{T}_x$ sheets, which can form a strong $\text{Ti}_3\text{C}_2\text{T}_x$ network with ideal rheological properties for layer by layer extrusion printing of independent 3D architectures [9]. The inks were used to fabricate interdigitated electrodes for micro-supercapacitors (MSCs) (Fig. 4f), which were endowed with very high specific surface areas by post-print freeze drying. The MSCs fabricated by this low-waste fabrication technique achieved high energy and power densities of $24.4 \mu\text{Wh cm}^{-2}$ and 0.64 mW cm^{-2} , respectively, at 4.3 mA cm^{-2} , showing great potential for the use of 3D-printed $\text{Ti}_3\text{C}_2\text{T}_x$ in future works. Figure 4a–c shows—concurrently with Fig. 2—that increasing the concentration of $\text{Ti}_3\text{C}_2\text{T}_x$ increases both the viscosity and elasticity of the system, which also shows shear thinning and yielding behaviour. $50 \text{ mg ml}^{-1} \text{ Ti}_3\text{C}_2\text{T}_x$ exhibited G'_{LVR} and σ_y^{Osc} values of 36.5 kPa and 206 Pa , respectively, and rapid switching between low (0.01 s^{-1}) and high (1000 s^{-1}) shear rates demonstrated shear thinning of four orders of magnitude, which quickly recovered when returned to low shear rate; ideal behaviour for DIW. To print the structures depicted in Fig. 4f, nozzles of $250 \mu\text{m}$ and $330 \mu\text{m}$ diameter were used, giving Ξ_G and Ξ_y values of $108\text{--}137$ and $0.61\text{--}0.77$, respectively. Although Ξ_y is less than 1 here, this would not have caused a practical issue so long as

the post-printing freeze drying step was carried out promptly [30–33].

Zhang et al. reported self-assembly of $\text{Ti}_3\text{C}_2\text{T}_x$ into a nematic liquid crystal phase suitable for wet spinning without using additives, adhesives or stabilising agents [17]. The study found that the nematic phase formed above a critical transition concentration, C_t , in multiple solvents, and that this critical concentration was related to the aspect ratio of the MXene flakes. Aqueous inks comprising large MXene flakes with a high aspect ratio (denoted L- $\text{Ti}_3\text{C}_2\text{T}_x$; $Z \approx 3.1 \mu\text{m}$) were studied alongside inks containing small MXene flakes with a lower aspect ratio (denoted S- $\text{Ti}_3\text{C}_2\text{T}_x$; $Z \approx 0.31 \mu\text{m}$), and it was found that although both inks were able to exhibit nematic phases with similar rheological behaviour, C_t was *ca.* $10 \times$ higher for S- $\text{Ti}_3\text{C}_2\text{T}_x$, and thus it had to be much more concentrated to reach the same viscosity and G'/G'' ratio as the L- $\text{Ti}_3\text{C}_2\text{T}_x$ ink (Fig. 5). It can also be seen in Fig. 5c that rheological behaviour and liquid crystal phase are directly linked, as there is a distinct change in the relationship between G'/G'' and oscillatory shear frequency, which is indicative of a transition from liquid-like to solid-like behaviour as the concentration is increased. Colloids with a concentration of 6.3 mg ml^{-1} —the lowest concentration at which nematic regions were observed with polarised light microscopy—was also the lowest concentration at which solid-like behaviour was seen.

Later work by Wang et al. employed formulations similar to those in their DIW work to make freeze-cast film electrodes

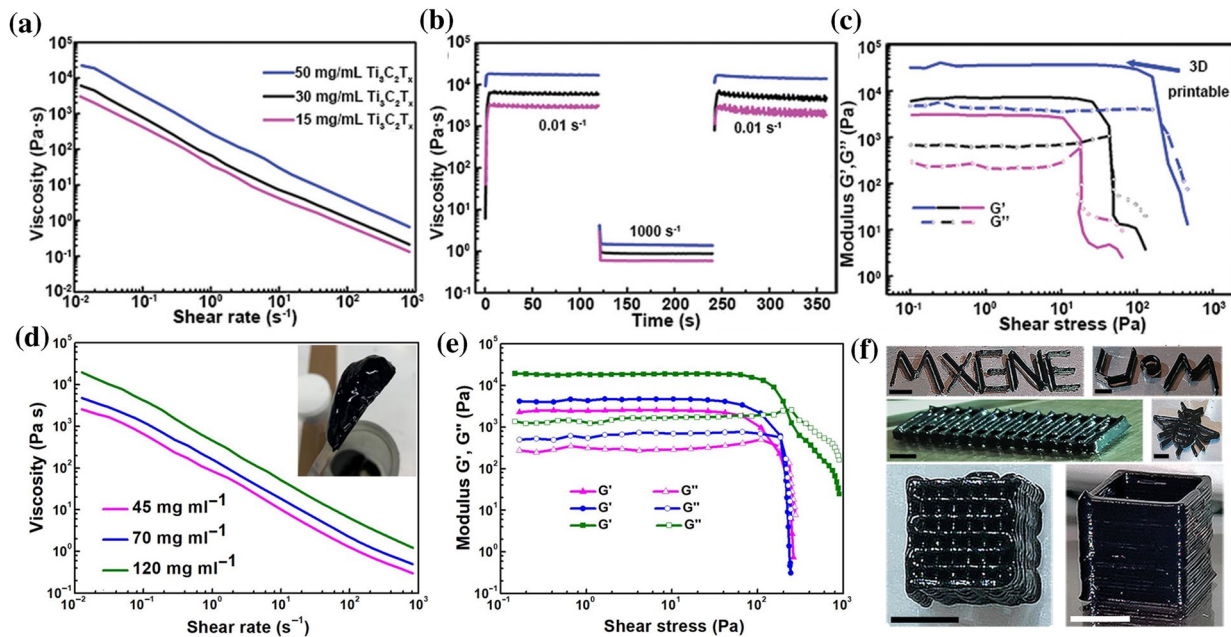


Figure 4: Similar formulations of aqueous $\text{Ti}_3\text{C}_2\text{T}_x$ reported by Yang, et al. in 2019 (*ca.* $8 \mu\text{m}$ flakes) (a–c, f) and 2020 (*ca.* $3.5 \mu\text{m}$ flakes) (d, e). (a, d) Viscosity vs. shear rate (η vs. $\dot{\gamma}$) of $\text{Ti}_3\text{C}_2\text{T}_{x(\text{aq})}$ at a range of concentrations (inset photograph of a 45 mg ml^{-1} sample). (b) Inks' viscosity evolution over time for alternate low (0.01 s^{-1}) and high shear rates (1000 s^{-1}), showcasing viscosity drop and recovery. (c, e) Viscoelastic moduli (G' and G'') as a function of oscillatory shear stress. (f) Photographs of 3D-printed $\text{Ti}_3\text{C}_2\text{T}_x$ structures made using $250\text{--}330 \mu\text{m}$ nozzles and printing speeds of $6\text{--}10 \text{ mm s}^{-1}$ (all scale bars 3 mm). Adapted with permission from Yang et al. [9, 34]. © 2019 & 2020 John Wiley and Sons.

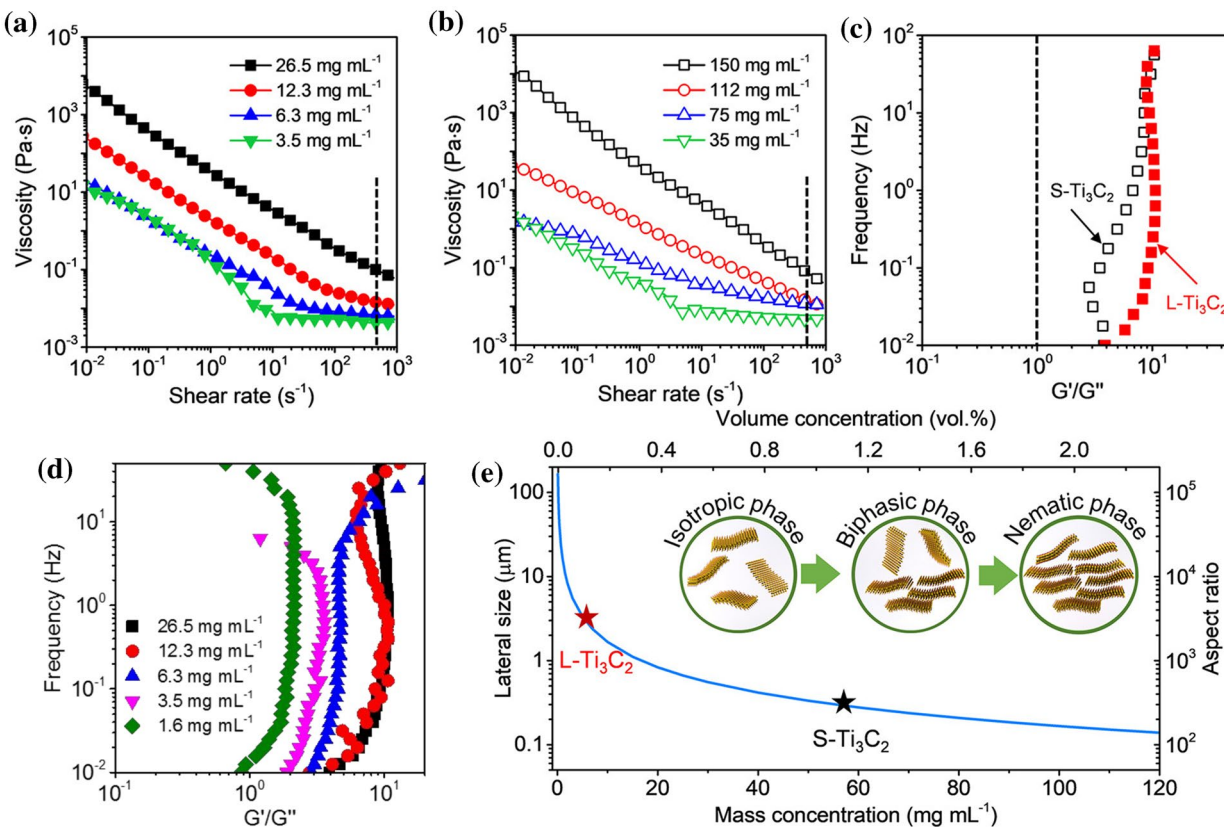


Figure 5: Rheological properties of S-Ti₃C₂T_x (*ca.* 0.31 μm flakes) and L-Ti₃C₂T_x (*ca.* 3.1 μm flakes) inks at various concentrations. Viscosity vs. shear rate of (a) 3.5 to 26.5 mg mL⁻¹ L-Ti₃C₂T_x inks and (b) 35 to 150 mg mL⁻¹ S-Ti₃C₂T_x inks. The black dashed lines in parts (a) and (b) indicate the shear rate applied during a wet spinning process to fabricate Ti₃C₂T_x fibres. (c), (d) The G'/G'' dependence on frequency for 26.5 mg mL⁻¹ L-Ti₃C₂T_x and 150 mg mL⁻¹ S-Ti₃C₂T_x (c), and 1.6–26.5 mg mL⁻¹ L-Ti₃C₂T_x inks (d). The dashed line at G'/G'' = 1 indicates the boundary between liquid- (<1) and solid-like (>1) behaviour. (e) Calculated phase diagram indicating the isotropic-nematic phase transition concentration for flakes of different sizes, including the experimentally determined transition concentrations of S-Ti₃C₂T_x and L-Ti₃C₂T_x. Adapted with permission from Zhang et al. [17]. © 2020 American Chemical Society.

[34]. However, this work employed Ti₃C₂T_x flakes with lateral sizes of only 3.7 μm (half that of the previous work), and just as was shown by Zhang et al. [17], this meant that higher concentrations were necessary to achieve comparable viscosity and viscoelastic moduli (Fig. 4d–e) [9, 34]. It should be noted that the effect of flake size on moduli and liquid crystal behaviour is consistent with effects seen in other 2D materials such as graphene oxide (GO), although the GO flakes used in many studies are 1–2 orders of magnitude larger than typical MXenes [17, 35, 36].

To achieve 3D DIW with small Ti₃C₂T_x flakes, Orangi, Shen et al. used different methods to increase the concentration of as-prepared aqueous dispersions [10, 29]. First, Orangi et al. increased the concentration of their Ti₃C₂T_x (*ca.* 10 mg mL⁻¹, Z ≈ 0.3 μm) using super absorbent polymer (SAP) beads, achieving concentrations of up to 290 mg mL⁻¹ (*ca.* 28.9 wt%). According to a Herschel-Bulkley fitting (black line in Fig. 6a), this facile technique created ink with a yield stress, σ_y , of 24 Pa (verified in Fig. 6b) and a flow index, n , of 0.73 ($n < 1$ indicates

shear thinning behaviour). A frequency sweep (Fig. 6c, d) was used to confirm that G'/G'' and G' > 10⁴ Pa at a wide range of timescales, and G'/G'' was in fact found to remain within the range deemed desirable for extrusion printing by Akuzum et al. (2–20) [11, 29]. DIW of MSC's was accomplished using 230–600 μm syringe tips. However, since the measured yield stress was only 24 Pa, no more than 10 layers could be printed. The photographs provided indicate that the printed layers merged together under the force of surface tension, γ_s , and after allowing them to dry at room temperature, the 1–10 layer structures shrank to 1.5–75 μm tall (though they maintained their original ‘footprint’ size and shape).

Soon afterwards, in their study of 3D-printed lithium anodes, Shen et al. reported reaching a similar concentration by vacuum filtration of 3.5 mg mL⁻¹ Ti₃C₂T_x (lateral size described as ‘several micrometres’, although only a single 1.5 μm flake measurement is clearly presented) [10]. The rheological data provided shows that the viscosity, η , of this ink decreases with a similar exponent to that presented by

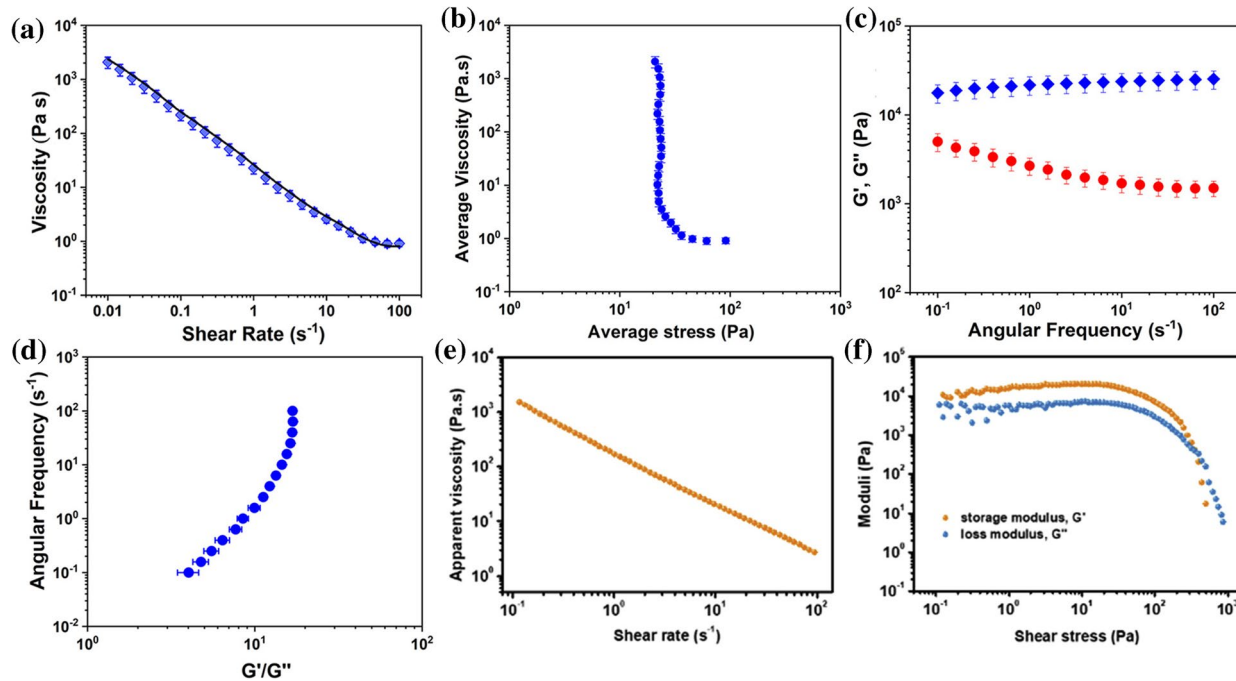


Figure 6: (a)–(d) Rheology of 290 mg ml⁻¹ $\text{Ti}_3\text{C}_2\text{T}_x$ (*ca.* 0.3 μm flakes) ink studied by Orangi, et al. (error bars represent standard error) [29]. Steady shear rheology: (a) viscosity (blue diamonds) and Herschel–Bulkley (line) model fit, and (b) the dramatic viscosity drop at the yield stress. Small amplitude oscillatory shear (SAOS) rheology: (c) G' (blue diamonds) and G'' (red circles) and (d) G'/G'' at 0.1–100 Hz. (e), (f) rheology of 300 mg ml⁻¹ $\text{Ti}_3\text{C}_2\text{T}_x$ (*ca.* 1.5 μm flakes) ink studied by Shen et al. [10] (e) Steady shear viscosity shows shear thinning, and (f) G' and G'' show yielding behaviour. Adapted with permission from Orangi, Shen et al. [10, 29]. © 2020 American Chemical Society and © 2020 Elsevier respectively.

Orangi et al., but with approximately 10× the viscosity at any given shear rate (Fig. 6a, e). The small strain storage modulus, G'_{LVR} , oscillatory yield stress, σ_y^{Osc} , and FTI were found to be 16.3 kPa, 365 Pa and 14, respectively, leading the ink to successfully be used in the DIW of 3D Li-plated $\text{Ti}_3\text{C}_2\text{T}_x$ electrodes.

Here, we have fitted the viscosity, η , data (measured in Pa s) discussed in this section to the simple equation

$$\eta \approx 1.1 \cdot Z^{1.5} C^{1.5} \dot{\gamma}^{-0.9} \equiv \eta_m, \quad (7)$$

where Z is the average $\text{Ti}_3\text{C}_2\text{T}_x$ flake diameter (measured in μm), C is the concentration of $\text{Ti}_3\text{C}_2\text{T}_x$ (measured in wt%), and $\dot{\gamma}$ is the applied shear rate (measured in s^{-1}). The accuracy of this fitting to different published datasets is presented in Fig. 7. Almost all of the data are accurately fitted by this model to within a factor of 2, with the exceptions being the data published by Zhang et al. [17], and the data on dilute colloids published by Akuzum et al. [11].

Regarding the measurements made by Akuzum et al., at the lowest concentration, Eq. (7) overestimates both the low-shear viscosity and the degree of shear thinning. However, for progressively higher concentrations, the shear thinning behaviour becomes better represented, and η_m overestimates η by a more consistent factor across the range of shear rates measured. Then, between the third and second highest concentrations measured

(1.8 and 2.7 mg ml⁻¹, *ca.* 0.18 and 0.27 wt%) there is an abrupt transition from $\eta_m/\eta \approx 30$ to $\eta_m/\eta \approx 1$, affirming the proposal that long-range order is achieved around this concentration [11].

With the information available, it is unclear why the data from J. Zhang et al. is fitted so poorly. Both the L- $\text{Ti}_3\text{C}_2\text{T}_x$ ($Z \approx 3.1 \mu\text{m}$) and S- $\text{Ti}_3\text{C}_2\text{T}_x$ ($Z \approx 0.31 \mu\text{m}$) datasets exhibit a similar ‘climb and drop’ in the η_m/η vs. C plot to the Akuzum et al. dataset, but the ‘drop’ (associated with the percolation threshold) is at a higher concentration than expected, given that L- $\text{Ti}_3\text{C}_2\text{T}_x$ flakes are *ca.* 3× larger than those used by Akuzum et al. Also of note is the difference in fitting between 1.2 and 2.6 wt% L- $\text{Ti}_3\text{C}_2\text{T}_x$: The viscosity of 2.6 wt% L- $\text{Ti}_3\text{C}_2\text{T}_x$ is *underestimated* by a factor of 3 at low shear rates and becomes accurate above *ca.* 10 s^{-1} , but the viscosity of 1.2 wt% L- $\text{Ti}_3\text{C}_2\text{T}_x$ is *overestimated* by a factor of 2 at low shear rate, and just becomes less accurate as the shear rate is increased. This is in contrast to the fittings of S- $\text{Ti}_3\text{C}_2\text{T}_x$ viscosities, which all become more accurate with increasing shear rate.

More work is needed to elucidate the causes of these discrepancies, test the limits of Eq. (7), and form a more accurate model of aqueous $\text{Ti}_3\text{C}_2\text{T}_x$ viscosity. To this end, future authors are encouraged to publish details of potentially significant factors such as the age of colloids at the time of measurement, their pH, the size distribution of MXene flakes, and their ζ -potential,

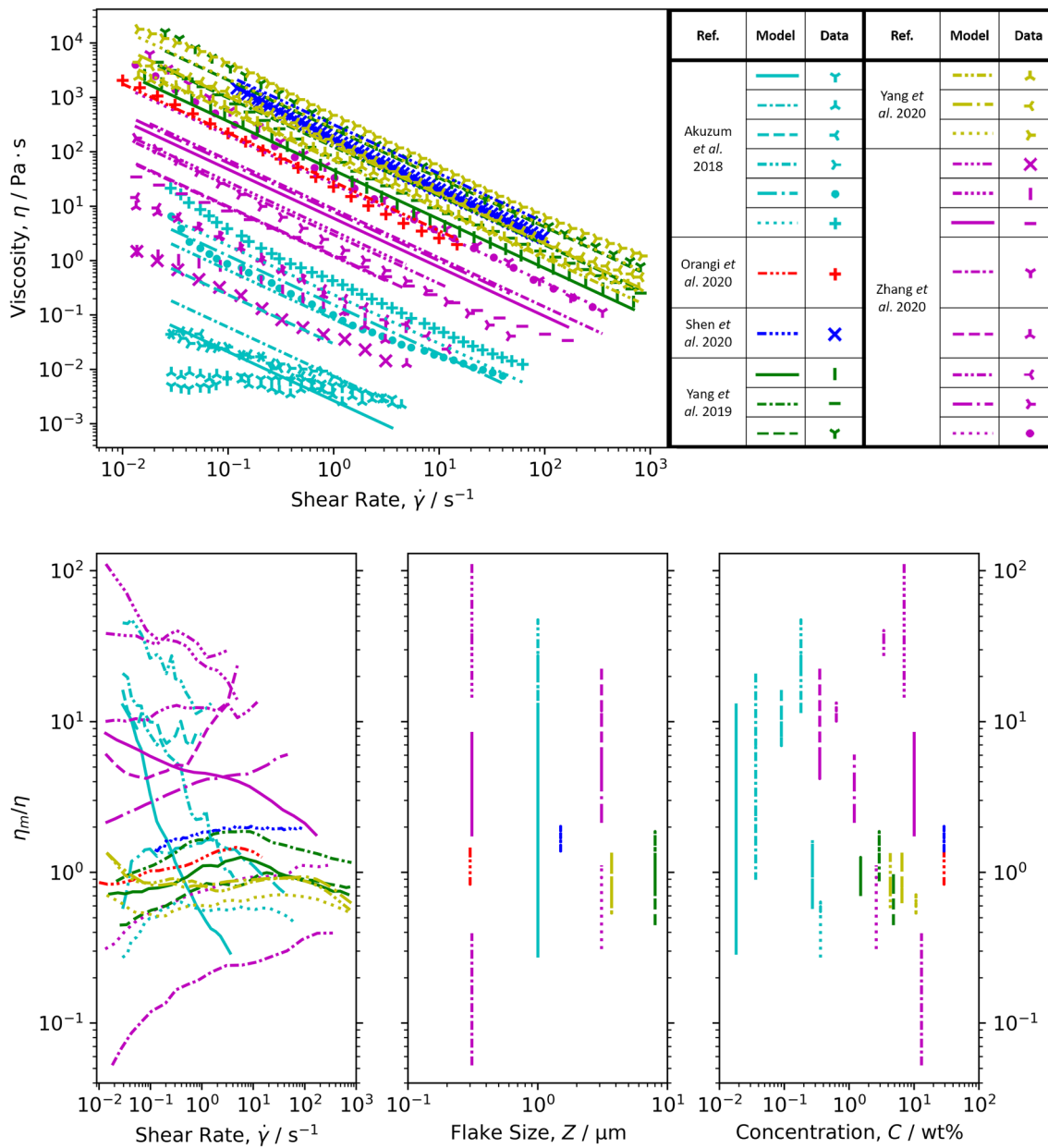


Figure 7: Published viscosity, η , data (symbols) [9–11, 17, 29, 34] plotted as a function of shear rate, $\dot{\gamma}$, alongside the viscosities predicted by Eq. (7), η_m . Below is the accuracy of η_m (measured as the quotient η_m/η) plotted as a function of the three parameters used in its calculation: $\dot{\gamma}$, Z and C .

which is a convenient parameter to use for approximating the strength of inter-particle forces. Once enough data are available, advanced computational methods could be used to advance both theoretical and practical understanding of MXenes' colloidal behaviour, and thus parameters could be optimised to achieve more efficient use of resources in commercial application [37].

To conclude this section, we make note of an issue which has not yet been addressed in any of the above work: the Cox-Merz rule, i.e. the correspondence between the steady state shear viscosity, η , and the magnitude of the complex viscosity, η^* ($= G^*/i\omega$, where ω is the angular frequency). The degree

of adherence to the Cox-Merz rule provides insight into the nature of colloidal microstructures under shear, and where it is adhered to, η or η^* can be predicted when only data on the other are available. For example, cone/plate rheometers often cannot reach the *ca.* 10^6 s⁻¹ steady shear rates experienced during inkjet printing[12] without unwanted sample ejection, so oscillatory shear could be used to estimate η at such a high rate. The Cox-Merz rule is not usually obeyed by colloidal dispersions, and as such it can only be applied to aqueous GO dispersions within a small concentration range (*ca.* 0.3–2 vol%) [26, 38]. However, we do not yet know whether

it applies to aqueous $\text{Ti}_3\text{C}_2\text{T}_x$, as the relevant data have not been published, even though it has presumably already been collected by everyone who has taken measurements of G^* and η as functions of ω and $\dot{\gamma}$.

Aqueous multilayer MXene

When Akuzum et al. studied aqueous colloids of multilayer $\text{Ti}_3\text{C}_2\text{T}_x$ particles ($Z \approx 5 \mu\text{m}$), they found that these also show

viscoelastic behaviour, but at much higher concentrations than monolayer $\text{Ti}_3\text{C}_2\text{T}_x$.^[11] At the highest concentration studied, 70 wt%, a low-shear viscosity of 1770 Pa s was measured, and shear thinning behaviour was observed at all concentrations (Fig. 8g). At low concentrations G'' dominates, but as the concentration increases G' becomes greater than G'' , and both increase by orders of magnitude, indicating a gel transition and percolation (Fig. 8a–f). This means that much like monolayer $\text{Ti}_3\text{C}_2\text{T}_x$ by changing the concentration of multilayer $\text{Ti}_3\text{C}_2\text{T}_x$, dispersions

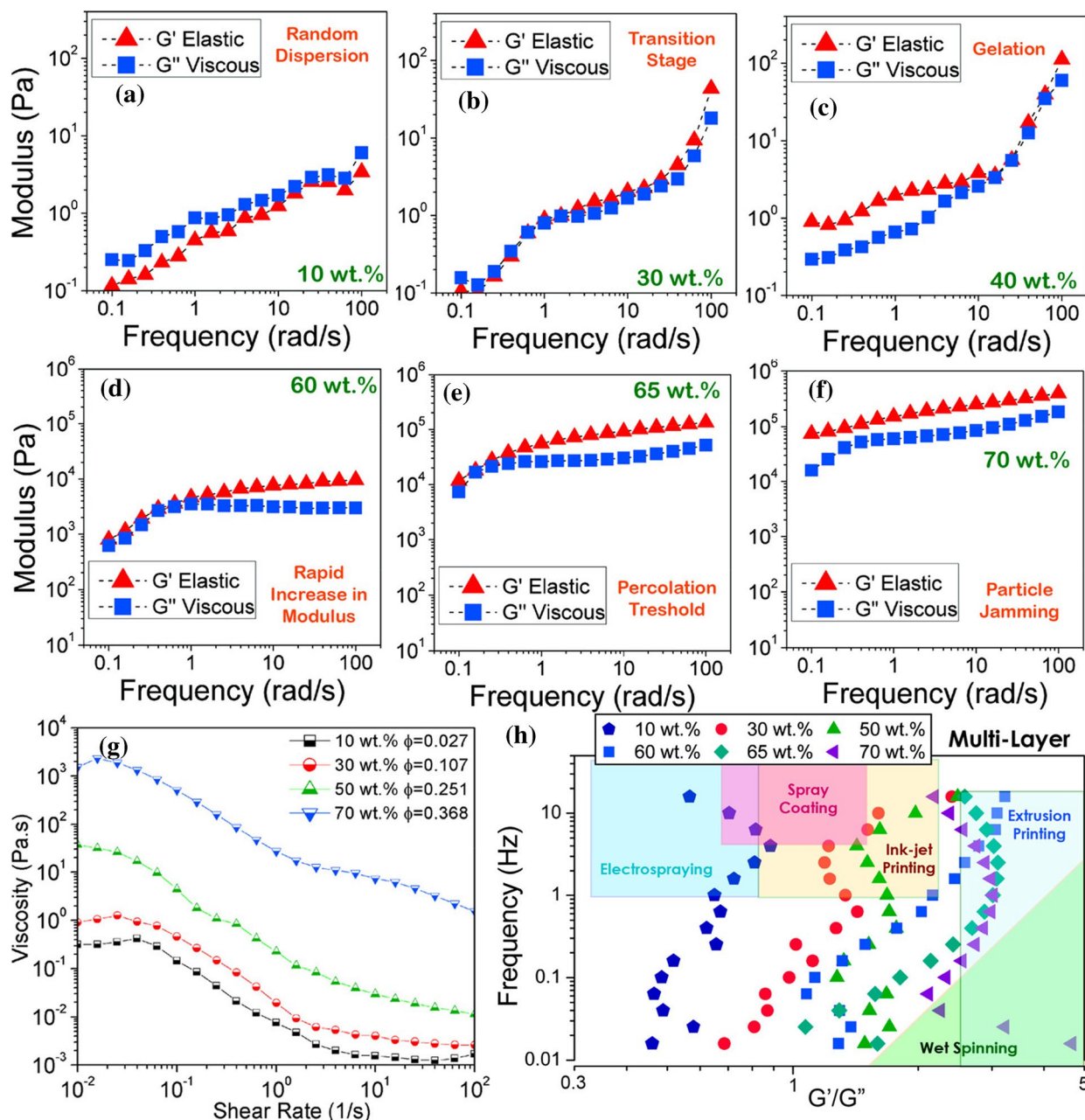


Figure 8: Viscoelastic behaviour of 10–70 wt% (volume fraction, ϕ , 2.7–36.8%) multilayer $\text{Ti}_3\text{C}_2\text{T}_x$ in water. (a–f) Frequency sweeps performed at 0.1% strain amplitude. (g) Viscosity vs. shear rate. (h) Frequency dependency of G'/G'' , and graph regions appropriate for typical fabrication processes. Adapted with permission from Akuzum, et al. [11]. © 2018 American Chemical Society.

can be made suitable for a wide range of applications such as electrospraying, spray coating, inkjet printing, extrusion printing and wet spinning (Fig. 8h). A key difference between the monolayer and multilayer $\text{Ti}_3\text{C}_2\text{T}_x$ studied by Akuzum et al. is that the multilayer $\text{Ti}_3\text{C}_2\text{T}_x$ was dried and redispersed, whereas the monolayer $\text{Ti}_3\text{C}_2\text{T}_x$ was kept wet from the start of the etching process. It is uncertain how much this will have affected the rheology, but it should be noted in case the drying process caused irreversible agglomeration and limited MXene-water interactions once the powder was redispersed [39].

Akuzum et al. suggested that multilayer $\text{Ti}_3\text{C}_2\text{T}_x$ might be more suitable for extrusion printing than monolayer because it presented higher elastic moduli, even though dispersions of monolayer $\text{Ti}_3\text{C}_2\text{T}_x$ with large values of G' were later 3D printed via extrusion (discussed above) [9, 10, 29]. The 3D shape of multilayer MXenes causes their packing behaviour to be very different to that of 2D monolayers, and the higher ζ -potential of monolayer particles causes them to have much stronger long-range interactions. This means that while comparable viscoelastic moduli can be reached at lower concentrations of monolayer $\text{Ti}_3\text{C}_2\text{T}_x$, their ability to flex and slide past each other even at high concentrations means that they continue to show viscoelastic yielding behaviour at moderate strain. In contrast, the movement of multilayer particles is more spatially hindered at high concentrations, and Akuzum et al. found G' dominated in 70 wt% multilayer $\text{Ti}_3\text{C}_2\text{T}_x$ over the entire frequency range tested, leading them to liken

it to a colloidal hard glass [11]. However, similar frequency-dependent behaviour can be seen with monolayer $\text{Ti}_3\text{C}_2\text{T}_x$ when comparing Fig. 8f to Fig. 5c, d and Fig. 6c. Therefore, it may be the case that multilayer $\text{Ti}_3\text{C}_2\text{T}_x$ is also printable by DIW at high concentrations, but an oscillatory shear amplitude sweep is necessary for a more complete comparison. As far as the authors of this review are aware, DIW of additive-free multilayer $\text{Ti}_3\text{C}_2\text{T}_x$ has not yet been achieved.

In light of the fact that both multi- and single-layer $\text{Ti}_3\text{C}_2\text{T}_x$ are able to act as rheology modifiers, Abdolhosseinzadeh et al. [40] investigated the screen printing of centrifugation sediment, which contains multilayer $\text{Ti}_3\text{C}_2\text{T}_x$ and un-etched Ti_3AlC_2 that would normally be considered waste from the MAX phase etching process. By mixing the sediment with 2 wt% monolayer $\text{Ti}_3\text{C}_2\text{T}_x$ (found in the centrifugation supernatant, $Z \approx 4 \mu\text{m}$), and then diluting the mixture to make a total solids mass loading of 22 wt%, a formulation capable of printing high resolution micro-supercapacitors, conductive tracks, and integrated circuit paths was achieved (Fig. 9e). The viscoelastic ink had a low-shear viscosity of 35 Pa s and a storage modulus of *ca.* 370 Pa (Fig. 9a, b), which increased by one and two orders of magnitude, respectively, when the ink had partially dried after printing (Fig. 9c, d). Notably, the drying effect of printing (which took the ink to *ca.* 34 wt% solids) had little effect on the oscillatory yield strain, γ_y^{Osc} , which remained at approximately 30–40%. This is because yielding occurs when the applied strain separates individual

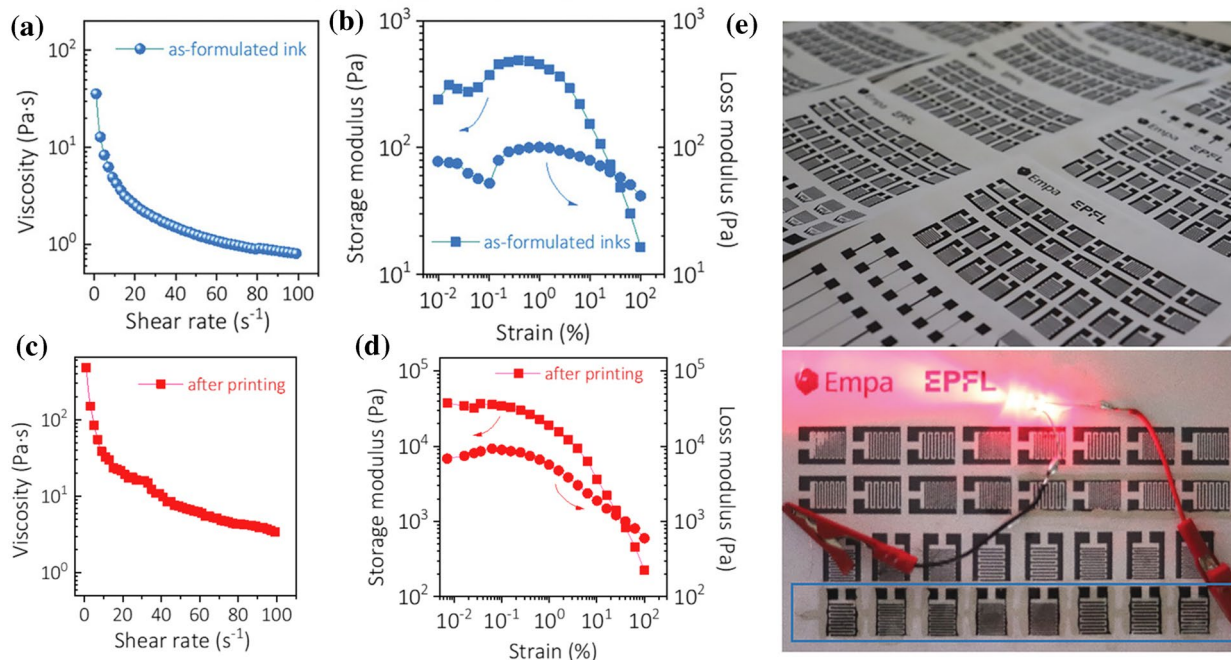


Figure 9: Rheology of MXene ink formulation by Abdolhosseinzadeh et al. before (a, b) and after (c, d) screen printing: (a, c) Viscosity vs. shear rate; (b, d) storage, G' , and loss, G'' , moduli vs. oscillatory shear strain amplitude at 0.5 Hz. (e) Photographs of screen-printed MSCs and a tandem device powering an LED light. Adapted with permission from Abdolhosseinzadeh et al. [40]. © 2020 John Wiley and Sons.

nanoparticles, causing the continuous, 3D network to break down.

MXene in non-aqueous solvents

While the majority of studies into MXenes have used water as their main solvent, stable dispersions of $\text{Ti}_3\text{C}_2\text{T}_x$ have been made with a number of other solvents, meaning they could be utilised in a wider range of potential applications and processing routes [6, 14, 41]. For example, Vural et al. were able to use dimethyl sulfoxide (DMSO)—which had previously been used to delaminate multilayer $\text{Ti}_3\text{C}_2\text{T}_x$ [42]—in the inkjet printing of $\text{Ti}_3\text{C}_2\text{T}_x$ -protein electrodes for stimuli-responsive electromagnetic shielding [43]. In this work, $\text{Ti}_3\text{C}_2\text{T}_x$ in DMSO (2.25 mg ml^{-1} , $Z \approx 3\text{--}6 \mu\text{m}$) exhibited Newtonian rheological behaviour, with a viscosity, η , of 3.1 mPa s across the entire shear rate range tested ($2\text{--}200 \text{ s}^{-1}$). This, along with a surface tension, γ_s , of 51.5 mN m^{-1} and a nozzle aperture, α , of $120 \mu\text{m}$ was used to assign $\text{Ti}_3\text{C}_2\text{T}_x$ in DMSO an inverse Ohnesorge number, $Z_O = \sqrt{\gamma_s \rho \alpha} / \eta$, of 27.48. Addition of a synthetic protein ('TR42', 0.95 mg ml^{-1}) enabled Z_O to reach 21.3, and although this is not within the generally accepted range for inkjet printing inks ($1 < Z_O < 14$), flexible electrodes with very high electrical conductivity ($1080 \pm 175 \text{ S cm}^{-1}$) were successfully printed onto a range of substrates.

Unlike Vural et al., Zhang et al.—who also developed organic $\text{Ti}_3\text{C}_2\text{T}_x$ formulations for inkjet printing—found viscoelastic behaviour in $\text{Ti}_3\text{C}_2\text{T}_x$ in DMSO, as well as in dispersions of $\text{Ti}_3\text{C}_2\text{T}_x$ in water, N-methyl-2-pyrrolidone (NMP), and

ethanol (Fig. 10) [4]. Examination of the publications suggests that the only significant difference between these two studies is that Vural et al. tested 2.25 mg ml^{-1} $\text{Ti}_3\text{C}_2\text{T}_x$ in DMSO, while C. Zhang et al. tested *ca.* 12 mg ml^{-1} $\text{Ti}_3\text{C}_2\text{T}_x$ in DMSO. Fig. 2a shows that dilute, shear thinning and aqueous dispersions of $\text{Ti}_3\text{C}_2\text{T}_x$ reach a viscosity plateau at a shear rate of *ca.* 1.5 s^{-1} , so it is reasonable to suggest that Vural et al. would have detected shear thinning if they had measured lower shear rates. The inks developed by C. Zhang et al. also showed much lower values of Z_O than those of Vural et al. (2.2–2.5), indicating that $\text{Ti}_3\text{C}_2\text{T}_x$ is a more effective viscosity modifier than TR42 protein. With no insulating binders, and a high concentration of $\text{Ti}_3\text{C}_2\text{T}_x$, C. Zhang et al. were able to report an extremely high conductivity in printed lines (up to 2770 S cm^{-1}) [4].

Overall, non-aqueous dispersions of $\text{Ti}_3\text{C}_2\text{T}_x$ appear to present similar rheology to their aqueous counterparts, although with lower absolute values of viscosity and viscoelastic moduli in accordance with the lower viscosities of the pure solvents. However, very little research has actually been published in this area, leaving much to be learned and much to be confirmed. It is important to expand our understanding of MXenes' behaviour in organic solvents, as it not only broadens the scope of possible applications, but also inhibits $\text{Ti}_3\text{C}_2\text{T}_x$ oxidation—a significant hindrance to commercial implementation—which seems to be expedited by water [44]. For example, a new application was recently investigated, as addition of *ca.* 0.1 wt\% $\text{Ti}_3\text{C}_2\text{T}_x$ increased the thermal conductivity of silicone and soybean oil by *ca.* 60%, and little degradation was observed over a period of 2 weeks [41, 45].

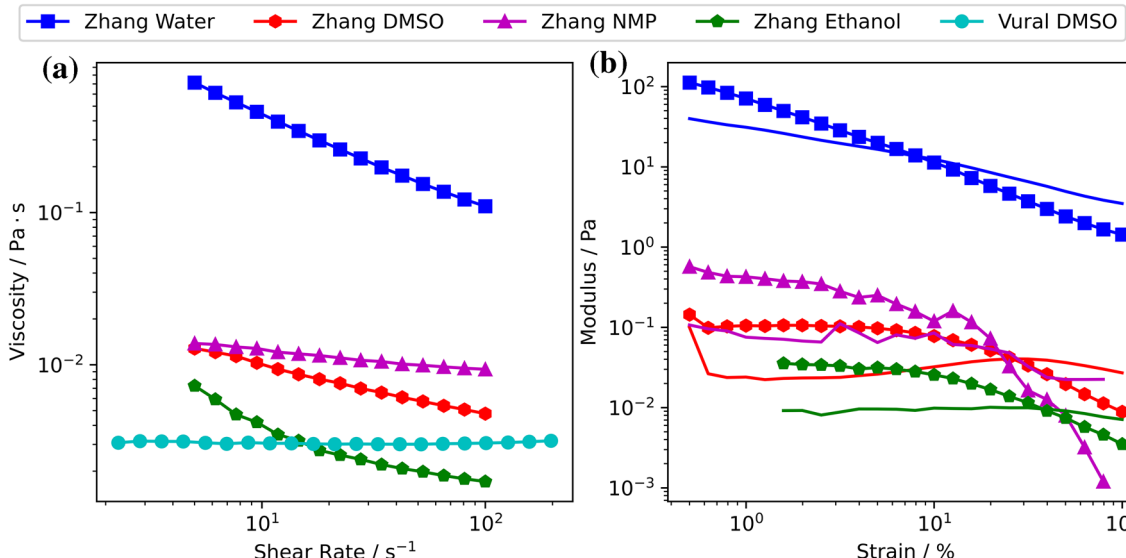


Figure 10: Rheological data gathered by Zhang [4], Vural [43], et al. on $\text{Ti}_3\text{C}_2\text{T}_x$ flakes dispersed in different solvents. (a) Viscosity as a function of shear rate. (b) Storage (G') and loss (G'') moduli as a function of oscillatory strain amplitude; G' is plotted with markers, and G'' is plotted without. The concentration of $\text{Ti}_3\text{C}_2\text{T}_x$ in water was 36 mg ml^{-1} , in ethanol was 0.7 mg ml^{-1} , and in NMP was 12 mg ml^{-1} . C. Zhang et al. measured 12 mg ml^{-1} $\text{Ti}_3\text{C}_2\text{T}_x$ in DMSO, while Vural et al. used 2.25 mg ml^{-1} .

With regards to the dispersion of MXene in molten polymers, a recent publication[46] examined the rheological properties of 0–1.0 wt% $\text{Ti}_3\text{C}_2\text{T}_x$ dispersed in thermoplastic polyurethane (TPU), using 0.5 wt% polyethylene glycol (PEG) as a dispersant. In parallel plate oscillatory frequency sweep experiments carried out at 200 °C (the temperature the authors also used for hot compression moulding), samples of all $\text{Ti}_3\text{C}_2\text{T}_x$ concentrations exhibited an increase of G' and G'' with increasing frequency, ω . However, the curves were less steep for higher MXene concentrations, such that these had higher moduli at low frequencies (≥ 0.01 Hz), and similar moduli at high frequencies (≤ 100 Hz). Congruently, the complex viscosity, η^* , was highest in samples with higher concentrations of MXene, but they showed different degrees of shear thinning, such that all samples exhibited $\eta^* \approx 200$ Pa s at $\omega = 100$ Hz. Unlike water, TPU is itself a shear thinning viscous fluid, like these low-concentration (sub-percolation threshold) $\text{Ti}_3\text{C}_2\text{T}_x$ composites, but addition of $\text{Ti}_3\text{C}_2\text{T}_x$ did increase the elastic component, decreasing G''/G' . In the frequency sweeps, a peak is observed in the value of G'/G'' , at *ca.* 1–3 Hz. Changes in the frequency of this peak for different $\text{Ti}_3\text{C}_2\text{T}_x$ mass loadings are attributed to the MXene's strong interactions with the TPU matrix, which has a microphase separation structure, and thus the flakes can interfere with energy dissipation (G'' is a measure of the energy lost as heat whilst under oscillatory shear). Higher concentrations

of $\text{Ti}_3\text{C}_2\text{T}_x$ have not yet been tested, and so it is not known whether this would cause the thermoplastic melt to become predominantly elastic.

Modified MXenes and composites

As discussed previously, the versatility of MXenes in device fabrication and implementation has made them especially effective when used as a conductive binder or scaffold to support other functional nanomaterials [3, 47]. For instance, Tang et al. synthesised S nanoparticles (mean diameter 34 nm) in a dilute suspension of monolayer $\text{Ti}_3\text{C}_2\text{T}_x$ ($Z \approx 2.6 \mu\text{m}$), which led to the self-assembly of a $\text{S}@\text{Ti}_3\text{C}_2\text{T}_x$ composite due to the species' opposite charges. After being washed and concentrated (to *ca.* 20 mg ml⁻¹), the aqueous composite was found to be almost as shear thinning as aqueous $\text{Ti}_3\text{C}_2\text{T}_x$ (Fig. 11a–c), and its $\dot{\gamma}$ (s⁻¹) vs. η (Pa s) relationship was fitted to the Ostwald–de Waele power law (cf. Eq. (7)):

$$\eta = K\dot{\gamma}^{n-1} \quad (8)$$

The Ostwald–de Waele relationship is a simple model to describe fluids using a 'flow consistency index', K , and a dimensionless 'flow behaviour index', n . The primary use of this model is to compare different fluids and make predictions, and the value of n indicates whether a fluid is shear thinning ($n < 1$), Newtonian ($n = 1$) or shear thickening ($n > 1$). However, it

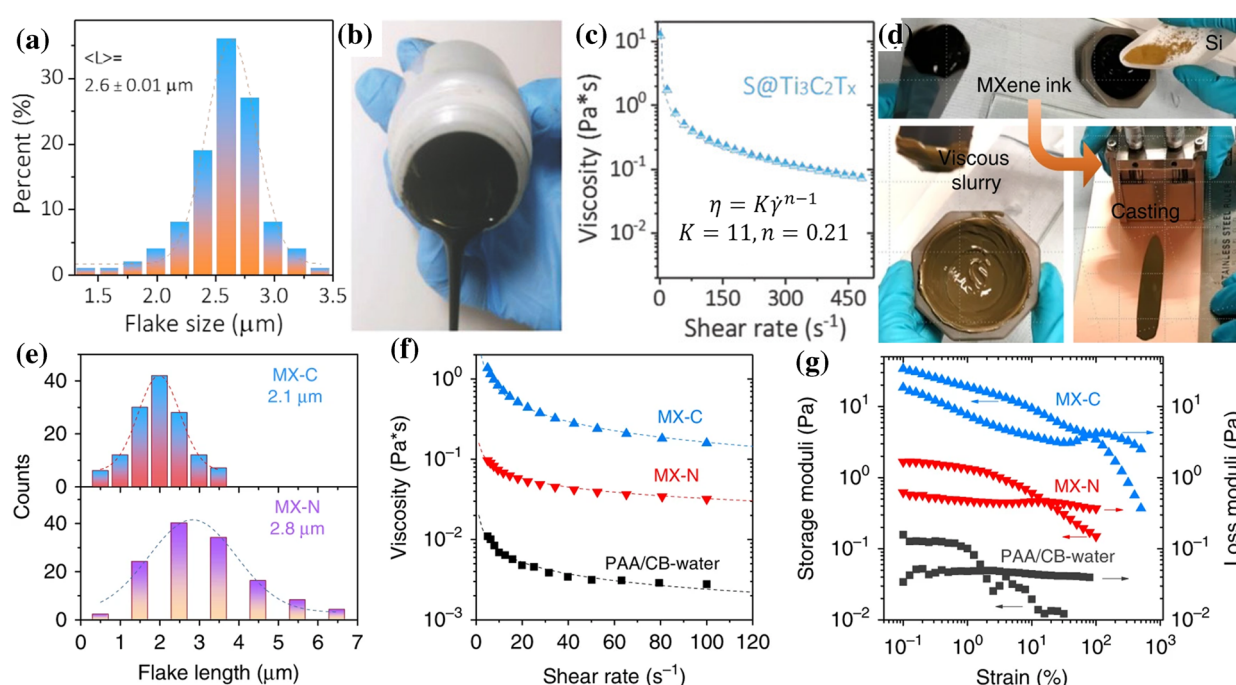


Figure 11: (a) $\text{Ti}_3\text{C}_2\text{T}_x$ lateral flake size histogram, (b) photograph, and (c) η – $\dot{\gamma}$ relationship of $\text{S}@\text{Ti}_3\text{C}_2\text{T}_x$ ink fabricated by Tang et al. [48] (d) Si/MXene composite electrode preparation, (e) histograms of $\text{Ti}_3\text{C}_2\text{T}_x$ (MX-C) and Ti_3CNT_x (MX-N) lateral flake sizes, and (f), (g) rheological properties of MX-C and MX-N inks prepared by Zhang et al.[49] Also included is a control sample made of polyacrylate and carbon black dispersed in water (PAA/CB-water). Adapted from Tang, Zhang et al. [48, 49] under a Creative Commons CC BY licence.

should be used with caution, as in cases where $n \neq 1$, η tends towards impossible values at extreme values of $\dot{\gamma}$, and so the model is only accurate over the range in which data were fitted.

With Parameters $K = 11$ and $n = 0.21$, the novel S@Ti₃C₂T_x composite could be painted or slurry cast—techniques which require high fluidity whilst force is being applied, but high viscosity when the material is left to rest—and applied directly onto Al foil and Celgard to fabricate high capacity, long-life Li–S batteries. The slurry could also be filtered to create flexible, free-standing membranes with a high tensile strength (*ca.* 12.9 MPa) and Young's modulus (*ca.* 19.2 GPa) [48].

Similarly, C. Zhang et al. demonstrated that Ti₃C₂T_x and Ti₃CNT_x can act as effective binders for Si and Si@graphene nanopowders (particle sizes *ca.* 80 nm and 10 μm , respectively) in the fabrication of thick ($\leq 450 \mu\text{m}$) Li-ion battery electrodes with areal capacities up to and including 23.3 mAh cm⁻². Ti₃C₂T_x was found to have the highest viscoelastic moduli, yield strain and viscosity, and 25 mg ml⁻¹ Ti₃C₂T_x, Ti₃CNT_x and polyacrylate/carbon black (PAA/CB) inks were shown to have Ostwald–de Waele parameters of $K = 3.25, 0.17$ and 0.022 , and $n = 0.35, 0.64$ and 0.52 , respectively (Fig. 11d–g). The ability of aqueous MXene to bind such thick electrodes and resist crack formation was directly attributed to the high measured values of these properties, which, as highlighted by the differences between Ti₃C₂T_x and Ti₃CNT_x, are related to the chemical structure of Ti₃C₂T_x, and not just a result of geometric effects. The 2D nature of delaminated MXenes necessitates that particle interactions are dominated by electrostatic forces, rather than jamming effects which dominate the rheology of multilayer MXenes, and therefore, the difference in ζ -potential between Ti₃C₂T_x and Ti₃CNT_x MXenes is a key piece of missing information that would help explain their differences in viscosity [11, 49].

Chemical modification can also be used to change the 3D microstructure of MXene structures, for example when crumpled, nitrogen-doped Ti₃C₂T_x (N-Ti₃C₂T_x) was prepared by Yu et al. [50] Here, melamine formaldehyde (MF) microspheres were mixed with a dilute suspension of delaminated Ti₃C₂T_x before being centrifuged, freeze-dried, and annealed to produce N-Ti₃C₂T_x powder. The powder was then mixed with carbon black, a polymer binder and water (solids 8:1:1 mass ratio, 27–34 wt% in water) to produce a screen printing ink (N-Ti₃C₂T_x/C), and with activated carbon (AC), carbon nanotubes (CNTs), GO and water to produce a DIW ink. The DIW ink (N-Ti₃C₂T_x/AC/CNT/GO) comprised N-Ti₃C₂T_x, AC, CNT and GO in a 3:3:2:4 mass ratio, and a control ink (AC/CNT/GO) comprised AC, CNT and GO in a 6:2:4 mass ratio. Their solids loadings were 15 wt% and 11 wt%, respectively.

The rheology of the inks presented by Yu et al. [50] is shown in Table 2. The 34 wt% N-Ti₃C₂T_x/C ink had a high viscosity at low shear rate, $\dot{\gamma}$, and G'_{LVR}/G''_{LVR} at low strain, meaning that

TABLE 2: Summary of rheological data found by Yu, J. Liang et al. regarding their aqueous composite inks used for screen printing and 3D DIW.

Aqueous formulation	Ref	$\eta(\text{low } \dot{\gamma}) / \text{Pa s}$	G'_{LVR} / Pa	$\sigma_y^{Osc} / \text{Pa}$ (FTI)	$\gamma_y^{Osc} / \%$
N-Ti ₃ C ₂ T _x /C 34 wt%	[50]	4.9×10^4	6.8×10^4	660 (5.5)	
N-Ti ₃ C ₂ T _x /C 31 wt%	[50]	7.8×10^3	1.2×10^4	92 (2.4)	
N-Ti ₃ C ₂ T _x /C 29 wt%	[50]	3.7×10^3	6.1×10^3	84 (1.5)	
N-Ti ₃ C ₂ T _x /C 27 wt%	[50]	4.8×10^2	5.3×10^2	83 (13.4)	
N-Ti ₃ C ₂ T _x /AC/CNT/GO 15 wt%	[50]	3.0×10^5	2.0×10^5	260 (2.0)	
AC/CNT/GO 11 wt%	[50]	2.0×10^5	1.1×10^5	74 (15.3)	
N-Ti ₃ C ₂ T _x /CNT/GO 23 wt%	[52]	7.7×10^3	9.0×10^3	130 (6.5)	
Ti ₃ C ₂ T _x	[53]	300	3.6×10^2	30	
Ti ₃ C ₂ T _x 80 mg ml ⁻¹	[54]	4.6×10^2	4.7×10^2	6	
Ti ₃ C ₂ T _x :AgNW 0.66:1.07 (vol%)	[55]	6.1×10^2	2.7×10^2	32	
Ti ₃ C ₂ T _x :AgNW 3:4 (w/w)	[53]	380	1.6×10^3	5	
Ti ₃ C ₂ T _x :AgNW 3:4 (w/w)	[54]	5.8×10^2	2.1×10^2	33	
RuO ₂ @Ti ₃ C ₂ T _x :AgNW 3:4 (w/w)	[53]	180	4.5×10^2	42	
Ti ₃ C ₂ T _x :AgNW:MnO ₂ 2NW 6:8:1 (w/w)	[54]	3.4×10^3	3.0×10^2	28	
Ti ₃ C ₂ T _x :AgNW:MnO ₂ W:C ₆₀ 30:40:5:2 (w/w)	[54]	1.5×10^3	4.4×10^2	47	

high resolution interdigitated electrodes could be printed. Looking through the rheology of N-Ti₃C₂T_x/C at a range of concentrations, it can be seen that a percolation threshold is present at *ca.* 28 wt%, above which G' and G'' change little with oscillation frequency, indicating the presence of a stable gel. As seen in Table 2, 15 wt% N-Ti₃C₂T_x/AC/CNT/GO had twice the storage modulus, 3.5× the yield stress and a much smaller FTI than 11 wt% AC/CNT/GO. This enabled *ca.* 15 mm tall structures to be extrusion printed with high resolution, using 190 μm and 260 μm diameter nozzles at a printing height of 0.15 mm. The printed filaments were on average 300 μm and 500 μm wide, respectively, before freeze drying, meaning the volume of the ink expanded by *ca.* 50% upon extrusion. No experiments were presented to directly compare the contributions from GO and CNTs to the rheology, although the authors do reference another work where a 26 wt% AC/CNT/GO ink demonstrated a yield stress and storage modulus of 1.7 kPa and 320 kPa, respectively [50, 51].

Later, the same group used a N-Ti₃C₂T_x/CNT/GO ink (5:2:3 mass ratio, 300 mg ml⁻¹ in water) and an AC/CNT/GO

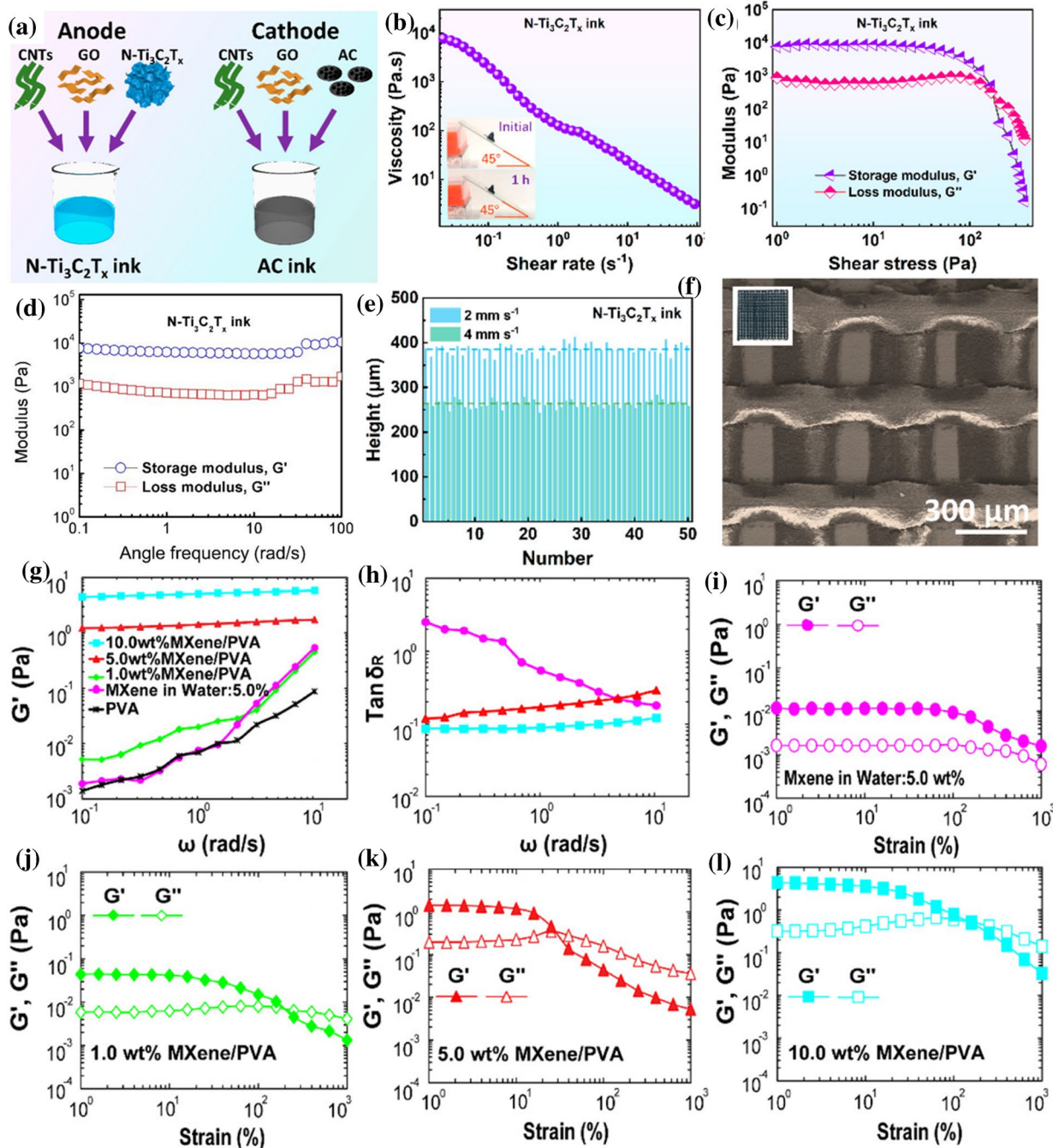


Figure 12: Rheological and fabrication data collected by (a–f) Fan et al. [52] and (g–l) Mirkhani et al. [57]. (a) Schematic diagram of the formulation of the anode and cathode inks. ‘ $\text{N-Ti}_3\text{C}_2\text{T}_x$ ink’ is referred to as ‘ $\text{N-Ti}_3\text{C}_2\text{T}_x/\text{CNT}/\text{GO}$ ’ in Table 2. (b) Apparent viscosity as a function of shear rate for the $\text{N-Ti}_3\text{C}_2\text{T}_x$ ink. (c–d) Viscoelastic moduli as a function of shear stress (c) and angular frequency (d) for the $\text{N-Ti}_3\text{C}_2\text{T}_x$ ink. (e) Height distribution of the $\text{N-Ti}_3\text{C}_2\text{T}_x$ ink lines achieved using a 200 μm diameter printing nozzle at 2 and 4 mm s^{-1} . (f) SEM image and photograph (inset) of the 3D-printed $\text{N-Ti}_3\text{C}_2\text{T}_x/\text{CNT}/\text{GO}$ woodpile electrode. (g) Storage modulus, G' , and (h) $\tan \delta_R = (G''/G')$ of different $\text{Ti}_3\text{C}_2\text{T}_x/\text{PVA}$ solutions in the oscillation frequency range 0.1–10 rad s^{-1} at 25 °C and constant strain (0.1%). (i–l) Oscillatory strain amplitude sweep response of $\text{Ti}_3\text{C}_2\text{T}_x$ MXene and $\text{Ti}_3\text{C}_2\text{T}_x/\text{PVA}$ solutions at 0.5 rad s^{-1} . MXene wt% shown is with respect to PVA, except for in the PVA-free solution, where it is with respect to water. PVA-containing solutions were made using 20 mg ml^{-1} aqueous PVA. Adapted with permission from Fan et al. [52] and Mirkhani et al. [57]. © 2020 & 2019 American Chemical Society.

ink (80:5:15 mass ratio, 600 mg ml^{-1} in water) to 3D-print the anodes and cathodes, respectively, of sodium ion hybrid capacitors (Fig. 12) [52]. Rheological tests (Table 2, Fig. 12b-d) showed that the $\text{N-Ti}_3\text{C}_2\text{T}_x/\text{CNT}/\text{GO}$ ink should be suitable for printing

small structures (*ca.* 1 cm tall), and this was achieved using a 200 μm diameter nozzle. Although both the inks expanded upon extrusion, especially when the needle was moved at a slower speed (Fig. 12e), the $\text{N-Ti}_3\text{C}_2\text{T}_x/\text{CNT}/\text{GO}$ ink expanded *ca.*

30% more than AC/CNT/GO, suggesting that it exhibits higher normal stresses due to its elasticity, but no data have yet been published on the normal stresses exhibited by MXene formulations under extrusion. Their bespoke 3D designs, and the pores formed thanks to the post-print freeze drying process and the crumpled $\text{N-Ti}_3\text{C}_2\text{T}_x$ particles, enable large amounts of Na^+ to quickly diffuse between the electrodes, increasing both the power and energy density of the electrodes; 102 Wh kg⁻¹ and 3.27 kW kg⁻¹ were achieved.

In their endeavours to print metal and metal oxide nanowire composites, Liang et al. have studied six aqueous combinations of $\text{Ti}_3\text{C}_2\text{T}_x$ MXene ($Z \approx 2\text{--}5 \mu\text{m}$) with Ag and MnO_2 nanowires (AgNW and MnO_2 NW), RuO_2 nanoparticles, and buckminsterfullerene (C_{60}) (Table 2) [53–55]. Not only is $\text{Ti}_3\text{C}_2\text{T}_x$ electrically conductive and electrochemically active, but rheological tests showed that it is also a much more effective rheology modifier than conventional additives such as poly(vinyl pyrrolidone). Just like aqueous MXene, all the mixtures shown were shear thinning, yielded at high strain, and had a short viscosity recovery time upon rapidly switching between low and high shear rates. Some studies were also carried out with *ca.* 1.5 μm GO flakes in place of $\text{Ti}_3\text{C}_2\text{T}_x$, and comparable rheological properties were achieved. As shown in Table 2, 80 mg ml⁻¹ aqueous $\text{Ti}_3\text{C}_2\text{T}_x$ prepared by J. Liang et al. demonstrated G'_{LVR} and η values on the order of 10² Pa/Pa s, which is *ca.* 10 \times less than similar formulations measured by Yang (Fig. 4d, e) [34], J. Zhang (Fig. 5a) [17], et al. This may be because J. Liang et al. freeze-dried their $\text{Ti}_3\text{C}_2\text{T}_x$ for storage before making their inks, leading to irreversible particle agglomeration [39].

Many studies have been done into MXene-polymer nanocomposites [56], but one in particular has used the rheological properties of aqueous MXene-polymer solution to elucidate the degree of dispersion between the composite components. As shown in Fig. 12, aqueous $\text{Ti}_3\text{C}_2\text{T}_x$ -poly(vinyl alcohol) (PVA) mixtures were compared to 5.0 wt% aqueous $\text{Ti}_3\text{C}_2\text{T}_x$ and 20 mg ml⁻¹ aqueous PVA (146–186 kDa) [57]. Figure 12g shows that the 5.0 wt% $\text{Ti}_3\text{C}_2\text{T}_x$ MXene and 20 mg ml⁻¹ PVA dispersions have similar frequency-dependent storage moduli, G' , and the mixture of PVA with 1.0 wt% MXene (wt% with respect to the PVA in solution) also shows similar behaviour, albeit with a higher low frequency storage modulus. This behaviour—along with the phase behaviour shown in Fig. 12h—is characteristic of a viscoelastic liquid, and it is not until the MXene reaches a concentration of 5 wt% (with respect to PVA) that a clear transition to gel-like behaviour is seen, indicating the presence of a continuous 3D structure within the sample. This gel transition seems to take place at a higher concentration than in other studies discussed in the present review, which may be because of interactions between the PVA and MXene flakes, but could evidence a small average MXene flake size (a detailed size distribution was not published).

Also unusual, is the lack of a yield strain, γ_y^{Osc} , in the oscillation amplitude sweep of 5.0 wt% MXene (Fig. 12i). The most likely explanation for this is that a yield strain exists beyond the tested range (1–1000%); however, it is still notable, as that would mean Mirkhani et al. have achieved a yield stress an order of magnitude greater than those in other works [4, 40, 49]. This may have been made possible by the unusual practice of bubbling inert gas through the reaction vessel during MAX phase etching, which prevents MXene oxidation ($\text{Ti}_3\text{C}_2\text{T}_x + [\text{O}] \rightarrow \text{TiO}_2 + \text{C}$), and therefore would increase the strength of MXene–water and MXene–MXene interactions. However, further testing is needed to confirm this.

The addition of progressively more $\text{Ti}_3\text{C}_2\text{T}_x$ to aqueous PVA is shown to increase G' by multiple orders of magnitude (Fig. 12j–l), but γ_y^{Osc} initially decreases and then increases as the MXene concentration goes from 1.0 to 5.0 to 10.0 wt%, and the 5.0 wt% MXene/PVA sample also exhibits a much more abrupt transition from linear elastic to non-linear viscous behaviour. Mirkhani et al. interpret this to mean that MXene-dominant and PVA-dominant transient structures easily form in the 10.0 wt% and 1.0 wt% MXene samples, respectively, but such structures are less easily formed when the MXene:PVA ratio is that used in Fig. 12k. These structures, which form and break cyclically under flow, are said to enable the 1.0 wt% and 10.0 wt% MXene structures to exhibit higher yield stresses. However, quantitative analysis of the unpublished oscillatory stress waveforms are needed to thoroughly investigate this claim [57, 58].

Another set of aqueous polymer–MXene dispersions studied recently is the polysaccharides hyaluronic acid (HA) sodium alginate (Alg) mixed in varying proportions with delaminated $\text{Ti}_3\text{C}_2\text{T}_x$ to enable 3D printing of human kidney cells. Unlike in other formulations, the addition of up to 5 mg ml⁻¹ $\text{Ti}_3\text{C}_2\text{T}_x$ ($Z \approx 1\text{--}4 \mu\text{m}$) to aqueous HA/Alg (5 wt% and 1 wt%, respectively) had little effect on the rheology, other than to increase G^* , σ_y and the speed of viscosity recovery upon rapidly switching from high to low shear rate. An aqueous colloid containing 5 mg ml⁻¹ $\text{Ti}_3\text{C}_2\text{T}_x$ demonstrated G'_{LVR} , G''_{LVR} , and σ_y values of 3.8, 1.6 and 2.2 kPa, respectively, as opposed to 2.0, 1.0 and 1.2 kPa as seen in an equivalent formulation with no $\text{Ti}_3\text{C}_2\text{T}_x$ [59].

Finally, Zhang et al. produced two smart materials with electro-responsive rheology by oxidising $\text{Ti}_3\text{C}_2\text{T}_x$ and Nb_2CT_x MXenes, and dispersing the resulting particles in oil [60, 61]. Upon application of an electric field, suspended electrorheological (ER) nanoparticles become aligned, and within one millisecond they can transform a colloid from a liquid-like to a solid-like material. Quick, reversible changes in viscosity and yield stress allow ER materials to be used in a wide range of applications such as in dampers, shock absorbers, microfluidics, clutches, and tactile displays. Here, $\text{Ti}_3\text{C}_2\text{T}_x$ and Nb_2CT_x were oxidised via different methods to create 3D nanoparticles with a range of morphologies, but the most distinct ER behaviour was seen

in colloids of albizia-like TiO_2/C in mineral oil, and lamellar $\text{Nb}_2\text{O}_5/\text{C}$ in silicone oil. Although both colloids initially showed Newtonian behaviour, application of electric fields caused them to exhibit Bingham plastic behaviour with viscoelastic moduli (G' , G''), a yield stress (σ_y), and an increased shear stress (σ) at given shear rates ($\dot{\gamma}$). The magnitudes of these values increased with concentration of the nanoparticles and the strength of the electric field. The great ER sensitivity of these materials is a result of polarisable metal oxides having good contact with conductive amorphous carbon, which thanks to the morphology of the particles has a high specific surface area to interact with the dielectric dispersant. The importance of particle morphology can be seen in a comparison of albizia-like and echeveria-like TiO_2/C particles. The albizia-like morphology allows both electrons and oil to flow more easily around each particle, and thus when an electric field is applied, the yield stress of a 5 vol% albizia- TiO_2/C colloid was shown to be higher than that of a 10 vol% echeveria- TiO_2/C colloid [60, 61].

Recommendations for future investigations

The publication of this review coincides with the tenth anniversary of the first isolation and characterisation of MXenes. Since then, the majority of research has been focussed their application, with less attention given to fundamental science. In a similar vein, this review has shown numerous publications reporting on the rheology of MXene-containing colloids to justify their use in methods such as extrusion and screen printing, but little experimental effort has been made to understand the physical principles behind this behaviour. To further the scientific community's understanding of MXene rheology, the authors of this review urge researchers to share much more data from the experiments which they are already doing. For example, a common pair of experiments is a sweep of linear shear rate and an oscillatory shear amplitude sweep, which demonstrate the shear thinning apparent viscosity, the viscoelastic moduli and the yield strain. But the results of these experiments can be presented in different ways to elucidate different properties, just as Orangi et al. have done in their presentation of the viscosity and yield stress of their $\text{Ti}_3\text{C}_2\text{T}_x$ ink (Fig. 6a, b)—more knowledge is shared without the need for further experimentation [29]. Similarly, in oscillatory shear measurements, most modern rheometers collect much more data than is commonly published. Alongside G' and G'' , oscillatory stress waveforms and values of properties such as normal force and complex viscosity, η^* , could be published. Publication of η^* would allow readers to deduce whether the Cox-Merz rule is applicable to MXene dispersions, and publication of oscillatory stress waveforms could help readers investigate

the microscopic interactions that dictate rheological behaviour in the non-linear regime (beyond γ_y^{Osc}). As discussed by Hyun et al., even qualitative analysis of stress waveforms could give insight into whether colloidal MXenes are behaving more like a continuous, structured gel, or a collection of many supramolecular structures whose close packing causes 'sticking and slipping' to occur as shear forces are applied [58].

The particle interactions that cause solid-like behaviour in MXene colloids can be separated into short-range and long-range interactions, which are analogous to the well-understood steric and electronic effects seen in molecular chemistry. The former are affected by properties such as particle size, shape and flexibility, and dominates the behaviour of 3D, multilayer $\text{Ti}_3\text{C}_2\text{T}_x$, which experiences jamming effects at high concentration in water, while the latter are affected by properties such as MXene chemistry (selection of metal carbide/nitride and surface terminations, T_x), solvent and salt concentration, and are a major influence in monolayer $\text{Ti}_3\text{C}_2\text{T}_x$ rheology [11]. The impact and the interplays between these parameters are as yet poorly understood, and warrant dedicated experimental investigation, but many of them—such as flake size—are also properties which should be measured in order to fully characterise any colloidal system which is being studied. Therefore, publication of the following parameters could enable systematic review to complement experimental investigations into rheology:

Particle size, shape, thickness and size distribution

As discussed in '[Aqueous single-layer MXene](#)', so long as $\text{Ti}_3\text{C}_2\text{T}_x$ is delaminated by a conventional method, the flakes will appear as random polygons of thickness ca. 2 nm (though this should of course be verified by atomic force microscopy (AFM) and electron microscopy). Thus, the most important properties to characterise in any given study are the lateral diameter, Z , and the 2D aspect ratio (the ratio of length to width, not length to thickness). These should both be graphically plotted in order to fully communicate the size distribution of flakes (Z typically follows a log-normal distribution), as this is likely to have a significant impact on colloidal rheology. For example, a small number of large flakes in a non-uniform sample may cause highly viscoelastic behaviour, and this effect would be undetectable in a study which simply quotes the average flake diameter. Where it is available, dynamic light scattering (DLS) can also be used as a convenient way to get an approximate size distribution, as it measures the hydrodynamic diameter of particles, which is approximately equal to Z in most cases, and may even accurately describe multilayer MXenes if they are roughly cubic [16–18]. Also of potential importance is *flake flexibility*, but this is understandably much more difficult to measure for most researchers.

Elemental composition, surface terminations (T_x), and sample age

The 2D nature of delaminated MXenes requires that their interaction in 3D space is highly dependent on long-range interactions, which are predominantly electrostatic. Therefore, the chemical make-up of MXenes significantly impacts their colloidal rheology [49], and this should be characterised as fully as possible. Whilst we accept that it is currently difficult to quantify the proportions and spatial arrangement of functional groups which are typically denoted with an ambiguous “ T_x ”, the present authors hope that developments in techniques such as hard X-ray photoelectron spectroscopy (HAXPES) will make the composition of MXenes better understood in the future [8, 16, 62–64]. As well as this, it is important to note the age of samples at the time of rheological measurement, because this will affect both the degree of oxidation (which decreases surface charge) and flocculation (which decreases surface charge and increases average particle size and shape) [65].

Ionic strength, pH

As well as the composition of the MXene itself, colloidal particle interactions are governed by their surrounding medium. As well as simply stating the solvent used (usually water in the case of MXenes), steps should be taken to get some indication of its ionic strength, which is a function of salt concentration, as this will affect the Debye screening length, which should be directly related to the strength of percolating networks which are thought to govern rheology (Equation (4)). Related to this is also the acidity of the solvent (or pH in the case of water), which determines the ratio of protonated and deprotonated alcohol termination groups ($-\text{OH}/-\text{O}^-$), affects what mixtures of termination groups are thermodynamically stable [66], and determines the favourability of either parallel and perpendicular flake stacking [8].

ζ -potential

As a property resulting from the sum of electrostatic forces acting on a nanoparticle surface, the ζ -potential of MXene flakes can shed light on many of the above properties which may be more difficult to measure, and is therefore one of the most important parameters that should be characterised. Knowing the ζ -potential of $\text{Ti}_3\text{C}_2\text{T}_x$ in a given sample (typically in the range -30 to -60 mV at neutral pH) [8, 24] gives insight into the strength of long-range, electrostatic particle interactions, and it is thus expected that inclusion of it in a model of colloidal viscosity could lead to a vast improvement upon Eq. (7). A common method employed to measure ζ -potential is DLS, and unfortunately this requires that samples be greatly diluted (ca. 0.1 wt% or 1 mg ml^{-1}), which alters the ionic strength of solution. To combat this, it is recommended that the concentration of salts in the concentrated colloid be as fully characterised as possible, and at least the pH be controlled, to make the electronic

environment of flakes in both concentrated and dilute samples as close as possible.

Conclusion

Even though there has only been one published work to systematically investigate the rheology of any MXene colloid (*Rheological Characteristics of 2D Titanium Carbide (MXene) Dispersions: A Guide for Processing MXenes*) [11], numerous works discussed in this review have since each contributed a small part to a greater understanding of how MXenes behave when dispersed at higher concentrations, with different nanomaterials and in different solvents. As Fig. 13 shows, $\text{Ti}_3\text{C}_2\text{T}_x$ MXene is an effective rheology modifier, enabling aqueous colloids to achieve high storage moduli, G' , and yield stresses, σ_y , at both low concentrations (in the case of monolayer $\text{Ti}_3\text{C}_2\text{T}_x$) and high concentrations (in the case of multilayer $\text{Ti}_3\text{C}_2\text{T}_x$), and it is therefore able to suit a wide range of applications.

Figure 13 contains graphene oxide (GO) data from two studies whose average flake diameters differ by almost a factor of 2 (64 μm vs. 37 μm) [26, 67], but despite this, their storage moduli closely fit to the same power law: $G' = 256 \cdot C^{2.94}$. It is thought that this consistency is due to the inverse relationship between flake diameter, Z and liquid crystalline behaviour [17], which allows colloidal 2D nanomaterials with Z larger than ca. 10 μm to exhibit similar rheological properties. The reverse argument can be used to at least partially explain the observed variation in colloidal $\text{Ti}_3\text{C}_2\text{T}_x$ rheological properties, as the studies referenced in Fig. 13 uses flakes with average Z values ranging from 0.3 to 8 μm . Despite the comparatively small size of the largest $\text{Ti}_3\text{C}_2\text{T}_x$ flakes studied ($Z \approx 8 \mu\text{m}$) [9], their colloids exhibited similar storage moduli to GO colloids with an average Z of 64 μm [26], indicating that the successful synthesis of larger MXene flakes may enable even higher G' values to be attained. Also, at all concentrations, the FTI of MXene-based formulations is very low—comparable to that of aqueous cellulose nanocrystals (CNCs)—meaning that inks with smaller yield stresses may still be 3D-printable.

On the topic of yield stresses, unlike GO or CNCs, the studied MXene-based formulations seem to hit a limit at ca. 300 Pa, which may also require larger flakes or gelling agents to be surpassed. But even in cases where other materials exhibit higher yield stresses, viscoelastic moduli or viscosities than $\text{Ti}_3\text{C}_2\text{T}_x$ colloids, few of them exhibit its versatility, conductivity and chemical activity. $\text{Ti}_3\text{C}_2\text{T}_x$ is dispersible in a wide range of polar solvents, including water [6], it greatly modifies colloidal rheology upon facile dispersion, and it does not require any post-processing treatment to achieve electrical conductivity comparable to graphene and chemical activity comparable to graphene oxide.

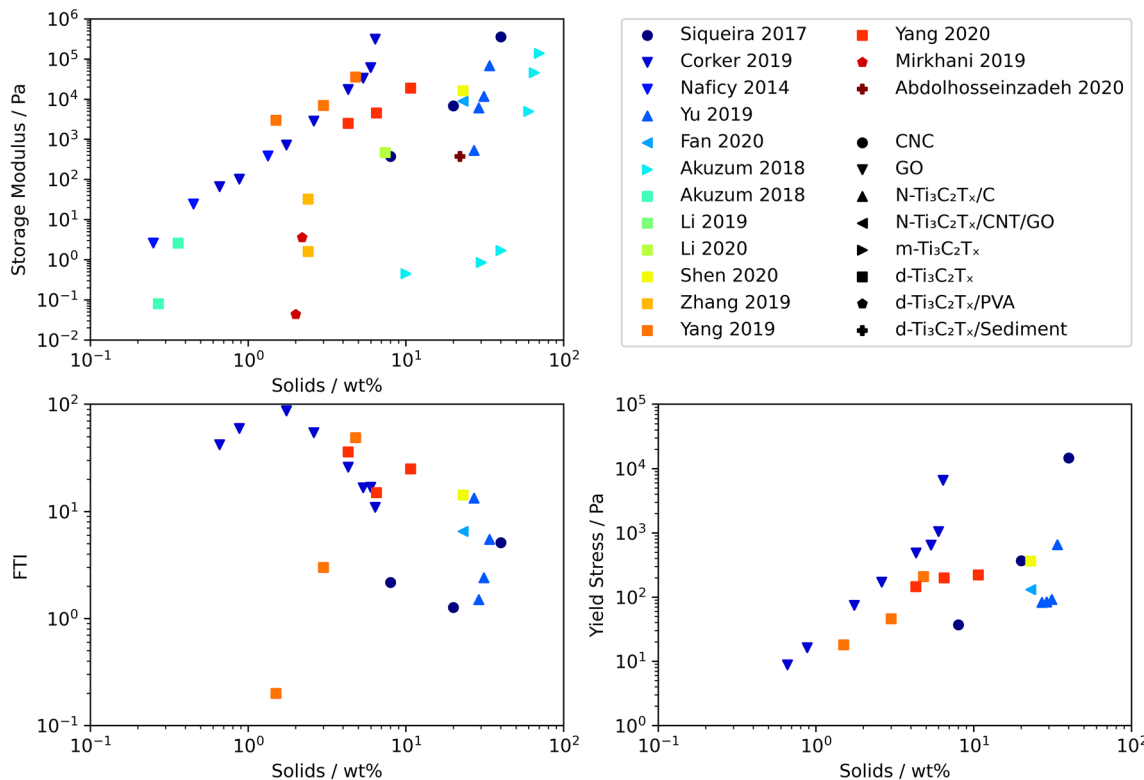


Figure 13: A graphical comparison of the storage modulus, G' , yield stress, σ_y , and flow transition indices (FTI) of aqueous colloids containing delaminated/monolayer $\text{Ti}_3\text{C}_2\text{T}_x$ (d- $\text{Ti}_3\text{C}_2\text{T}_x$) [9–11, 34, 49, 53, 54], multilayer $\text{Ti}_3\text{C}_2\text{T}_x$ (m- $\text{Ti}_3\text{C}_2\text{T}_x$) [11], cellulose nanocrystals (CNC) [68], graphene oxide (GO) [26, 67] and mixtures of d- $\text{Ti}_3\text{C}_2\text{T}_x$ or N-doped $\text{Ti}_3\text{C}_2\text{T}_x$ (N-Ti₃C₂T_x) with other materials [40, 50, 52, 57].

Delaminated 2D materials impact colloidal rheology via strong electrostatic interactions, and so the chemical structure of MXene flakes must play an important role—whether that is in the choice of metal carbide/nitride itself [49], in the selection of surface terminations (T_x), or in the degree of flake oxidation [57]—but these properties have not yet been systematically compared with respect to rheology; not least the choice of metal carbide/nitride, as no MXene has to date received anywhere near as much attention as $\text{Ti}_3\text{C}_2\text{T}_x$. As well as this, since $\text{Ti}_3\text{C}_2\text{T}_x$ flakes are positively charged at the edges, and negatively charged on their surface, more investigation is needed to see how electrostatic parameters, such as salt concentration and pH, might disrupt or enhance the percolating network to alter colloid rheology [8].

Looking then to multilayer MXenes, the shift in dominance from electrostatic to jamming effects would imply that chemical structure is less important, and so different MXenes could be used, or even composited with other materials, to achieve similar rheology to that presented by Akuzum et al. [11]. This proposal has not yet been tested, but if correct it could significantly broaden the applicability of multilayer MXenes to novel processing routes and devices.

As this review shows, many publications have reported on the rheology—specifically the apparent viscosities and viscoelastic

moduli—of MXene-containing colloids to justify their application in colloidal processing, but very little has been done to understand the physical principles behind the behaviour. On the one hand, more dedicated rheological studies are needed to investigate the interplays between shear field, particle geometry and surface chemistry. But on the other, significant insights could be gained by future systematic reviews if researchers shared more data from the rheological experiments they are already doing. For example, many papers show changes in G' and G'' as a function of either stress or strain, and this data have usually been collected under the oscillatory shear imposed by either a cone and plate or parallel plate shear rheometer. During these experiments, other data are often collected by the rheometer (such as oscillatory stress waveforms), but is not published. If it were, then analysis of that data could provide insight into things such as the transition from the linear to the non-linear regime (beyond γ_y^{osc}), or the way particles interact to form larger structures, and the way those structures interact under shear [58]. The additional knowledge gained from this data, as well as that gained from details such as the measurement temperature, the pH and age of samples, and the ζ -potential of MXene flakes, could also be used to further develop empirical models of aqueous $\text{Ti}_3\text{C}_2\text{T}_x$ rheology, improving upon η_m (Eq. (7)), along with models of other properties, such as G' and γ_y . As MXenes find usefulness in a growing range of applications, a

better understanding of their colloidal rheology will help ensure their future in commercial technology.

Author contributions

Conceptualization: SB, MG, JW, and WY; Methodology: MG; Formal Analysis: MG; Investigation: MM and MG; Writing—Original Draft: MG; Writing—Review & Editing: SB and MG; Visualisation: MG; Project administration: MG, SB; Supervision: SB; Funding Aquisition: SB.

Funding

This work was supported by the Graphene NOWNANO CDT, through EPSRC Grant (EP/L01548X/1), and Heilongjiang Huasheng Graphite Co. Ltd.

Declarations

Conflict of interest The authors have no relevant financial or non-financial interests to disclose.

Open Access

This article is licensed under a Creative Commons Attribution 4.0 International License, which permits use, sharing, adaptation, distribution and reproduction in any medium or format, as long as you give appropriate credit to the original author(s) and the source, provide a link to the Creative Commons licence, and indicate if changes were made. The images or other third party material in this article are included in the article's Creative Commons licence, unless indicated otherwise in a credit line to the material. If material is not included in the article's Creative Commons licence and your intended use is not permitted by statutory regulation or exceeds the permitted use, you will need to obtain permission directly from the copyright holder. To view a copy of this licence, visit <http://creativecommons.org/licenses/by/4.0/>.

References

- Q. Song, F. Ye, L. Kong, Q. Shen, L. Han, L. Feng et al., Graphene and MXene nanomaterials: toward high-performance electromagnetic wave absorption in gigahertz band range. *Adv. Funct. Mater.* **30**, 2000475 (2020). <https://doi.org/10.1002/adfm.20200475>
- S. Tagliaferri, A. Panagiotopoulos, C. Mattevi, Direct ink writing of energy materials. *Mater. Adv.* (2021). <https://doi.org/10.1039/DOMA00753F>
- G. Tontini, M. Greaves, S. Ghosh, V. Bayram, S. Barg, MXene-based 3D porous macrostructures for electrochemical energy storage. *J. Phys. Mater.* **3**, 022001 (2020). <https://doi.org/10.1088/2515-7639/ab78f1>
- C. Zhang, L. McKeon, M.P. Kremer, S.H. Park, O. Ronan, A. Seral-Ascaso et al., Additive-free MXene inks and direct printing of micro-supercapacitors. *Nat. Commun.* **10**, 1795 (2019). <https://doi.org/10.1038/s41467-019-09398-1>
- L. Verger, C. Xu, V. Natu, H.M. Cheng, W. Ren, M.W. Barsoum, Overview of the synthesis of MXenes and other ultrathin 2D transition metal carbides and nitrides. *Curr. Opin. Solid State Mater. Sci.* **23**, 149–163 (2019). <https://doi.org/10.1016/j.cossc.2019.02.001>
- K. Maleski, V.N. Mochalin, Y. Gogotsi, Dispersions of two-dimensional titanium carbide MXene in organic solvents. *Chem. Mater.* **29**, 1632–1640 (2017). <https://doi.org/10.1021/acs.chemmater.6b04830>
- C.A. Voigt, M. Ghidiu, V. Natu, M.W. Barsoum, Anion adsorption, Ti₃C₂Tz MXene multilayers, and their effect on claylike swelling. *J. Phys. Chem. C* **122**, 23172–23179 (2018). <https://doi.org/10.1021/acs.jpcc.8b07447>
- V. Natu, M. Sokol, L. Verger, M.W. Barsoum, Effect of edge charges on stability and aggregation of Ti₃C₂Tz MXene colloidal suspensions. *J. Phys. Chem. C* **122**, 27745–27753 (2018). <https://doi.org/10.1021/acs.jpcc.8b08860>
- W. Yang, J. Yang, J.J. Byun, F.P. Moissinac, J. Xu, S.J. Haigh et al., 3D printing of freestanding MXene architectures for current-collector-free supercapacitors. *Adv. Mater.* **31**, 1902725 (2019). <https://doi.org/10.1002/adma.201902725>
- K. Shen, B. Li, S. Yang, 3D printing dendrite-free lithium anodes based on the nucleated MXene arrays. *Energy Storage Mater.* **24**, 670–675 (2020). <https://doi.org/10.1016/j.ensm.2019.08.015>
- B. Akuzum, K. Maleski, B. Anasori, P. Lelyukh, N.J. Alvarez, E.C. Kumbur et al., Rheological characteristics of 2D titanium carbide (MXene) dispersions: a guide for processing MXenes. *ACS Nano* **12**, 2685–2694 (2018). <https://doi.org/10.1021/acsnano.7b08889>
- S. Uzun, M. Schelling, K. Hantanasirisakul, T.S. Mathis, R. Askeland, G. Dion et al., Additive-free aqueous MXene inks for thermal inkjet printing on textiles. *Small* **17**, 2006376 (2021). <https://doi.org/10.1002/smll.202006376>
- A. Saleh, S. Wustoni, E. Bihar, J.K. El-Demellawi, Y. Zhang, A. Hama et al., Inkjet-printed Ti₃C₂Tx MXene electrodes for multimodal cutaneous biosensing. *J. Phys. Mater.* **3**, 044004 (2020). <https://doi.org/10.1088/2515-7639/abb361>
- L. Das, K. Habib, R. Saidur, N. Aslfattahi, S.M. Yahya, F. Rubbi, Improved thermophysical properties and energy efficiency of aqueous ionic liquid/MXene nanofluid in a hybrid PV/T solar system. *Nanomaterials* **10**, 1372 (2020). <https://doi.org/10.3390/nano10071372>
- S. Abdolhosseinzadeh, X. Jiang, H. Zhang, J. Qiu, C. Zhang, Perspectives on solution processing of two-dimensional MXenes. *Mater. Today* (2021). <https://doi.org/10.1016/j.mattod.2021.02.010>
- M. Alhabeb, K. Maleski, B. Anasori, P. Lelyukh, L. Clark, S. Sin et al., Guidelines for synthesis and processing of

- two-dimensional titanium carbide (Ti₃C₂Tx MXene). *Chem. Mater.* **29**, 7633–7644 (2017). <https://doi.org/10.1021/acs.chemmater.7b02847>
17. J. Zhang, S. Uzun, S. Seyedin, P.A. Lynch, B. Akuzum, Z. Wang et al., Additive-free MXene liquid crystals and fibers. *ACS Cent. Sci.* **6**, 254–265 (2020). <https://doi.org/10.1021/acscentsci.9b01217>
 18. K. Maleski, C.E. Ren, M.-Q. Zhao, B. Anasori, Y. Gogotsi, Size-dependent physical and electrochemical properties of two-dimensional MXene flakes. *ACS Appl. Mater. Interfaces* **10**, 24491–24498 (2018). <https://doi.org/10.1021/acsami.8b04662>
 19. N. Phan-Thien, *Understanding Viscoelasticity*, 3rd edn. (Springer, Cham, 2003)
 20. Cunningham N. Essential tools for the new Rheologist. TA Webinars 2016. <https://www.tainstruments.com/neil-cunningham-essential-tools-for-the-new-rheologist/>.
 21. S.M. Jorgun, C.F. Zukoski, Rheology and microstructure of dense suspensions of plate-shaped colloidal particles. *J Rheol (N Y)* **43**, 847–871 (1999). <https://doi.org/10.1122/1.551013>
 22. R. Buscall, J.W. Goodwin, M.W. Hawkins, R.H. Ottewill, Viscoelastic properties of concentrated lattices. Part 1—Methods of examination. *J. Chem. Soc. Faraday Trans.* **78**, 2873 (1982). <https://doi.org/10.1039/f19827802873>
 23. S.A. Shah, T. Habib, H. Gao, P. Gao, W. Sun, M.J. Green et al., Template-free 3D titanium carbide (Ti₃C₂Tx) MXene particles crumpled by capillary forces. *Chem. Commun.* **53**, 400–403 (2017). <https://doi.org/10.1039/c6cc07733a>
 24. Y. Ying, Y. Liu, X. Wang, Y. Mao, W. Cao, P. Hu et al., Two-dimensional titanium carbide for efficiently reductive removal of highly toxic chromium(VI) from water. *ACS Appl. Mater. Interfaces* **7**, 1795–1803 (2015). <https://doi.org/10.1021/am5074722>
 25. E. Quain, T.S. Mathis, N. Kurra, K. Maleski, K.L. Van Aken, M. Alhabeb et al., Direct writing of additive-free MXene-in-water ink for electronics and energy storage. *Adv. Mater. Technol.* **4**, 1800256 (2019). <https://doi.org/10.1002/admt.201800256>
 26. A. Corker, H.C.H. Ng, R.J. Poole, E. García-Tuñón, 3D printing with 2D colloids: designing rheology protocols to predict “printability” of soft-materials. *Soft Matter* **15**, 1444–1456 (2019). <https://doi.org/10.1039/c8sm01936c>
 27. A. M'Barki, L. Bocquet, A. Stevenson, Linking rheology and printability for dense and strong ceramics by direct ink writing. *Sci. Rep.* **7**, 6017 (2017). <https://doi.org/10.1038/s41598-017-06115-0>
 28. B. Géraud, L. Jørgensen, L. Petit, H. Delanoë-Ayari, P. Jop, C. Barentin, Capillary rise of yield-stress fluids. *Europhys. Lett.* **107**, 58002 (2014). <https://doi.org/10.1209/0295-5075/107/58002>
 29. J. Orangi, F. Hamade, V.A. Davis, M. Beidaghi, 3D printing of additive-free 2D Ti₃C₂Tx (MXene) ink for fabrication of micro-supercapacitors with ultra-high energy densities. *ACS Nano* **14**, 640–650 (2020). <https://doi.org/10.1021/acsnano.9b07325>
 30. E. Koos, N. Willenbacher, Capillary forces in suspension rheology. *Science* **331**, 897–900 (2011). <https://doi.org/10.1126/science.1199243>
 31. S. Roh, D.P. Parekh, B. Bharti, S.D. Stoyanov, O.D. Velev, 3D printing by multiphase silicone/water capillary inks. *Adv Mater* **29**, 1701554 (2017). <https://doi.org/10.1002/adma.201701554>
 32. E. García-Tuñón, S. Barg, J. Franco, R. Bell, S. Eslava, E. D'Elia et al., Printing in three dimensions with graphene. *Adv. Mater.* **27**, 1688–1693 (2015). <https://doi.org/10.1002/adma.201405046>
 33. J.A. Lewis, Direct ink writing of 3D functional materials. *Adv. Funct. Mater.* **16**, 2193–2204 (2006). <https://doi.org/10.1002/adfm.200600434>
 34. W. Yang, J.J. Byun, J. Yang, F.P. Moissinac, Y. Peng, G. Tontini et al., Freeze-assisted tape casting of vertically aligned mxene films for high rate performance supercapacitors. *ENERGY Environ. Mater.* (2020). <https://doi.org/10.1002/eem2.12106>
 35. E. García-Tuñón, E. Feilden, H. Zheng, E. D'Elia, A. Leong, E. Saiz, Graphene oxide: an all-in-one processing additive for 3D printing. *ACS Appl. Mater. Interfaces* **9**, 32977–32989 (2017). <https://doi.org/10.1021/acsami.7b07717>
 36. J. Chen, F. Chi, L. Huang, M. Zhang, B. Yao, Y. Li et al., Synthesis of graphene oxide sheets with controlled sizes from sieved graphite flakes. *Carbon N Y* **110**, 34–40 (2016). <https://doi.org/10.1016/j.carbon.2016.08.096>
 37. L. Deng, B. Feng, Y. Zhang, An optimization method for multi-objective and multi-factor designing of a ceramic slurry: Combining orthogonal experimental design with artificial neural networks. *Ceram. Int.* **44**, 15918–15923 (2018). <https://doi.org/10.1016/j.ceramint.2018.06.010>
 38. C. Vallés, R.J. Young, D.J. Lomax, I.A. Kinloch, The rheological behaviour of concentrated dispersions of graphene oxide. *J. Mater. Sci.* **49**, 6311–6320 (2014). <https://doi.org/10.1007/s10853-014-8356-3>
 39. J.H. Adair, E. Suvaci, J. Sindel, *Surface and Colloid Chemistry* (Elsevier, Amsterdam, 2001), pp. 1–10
 40. S. Abdolhosseinzadeh, R. Schneider, A. Verma, J. Heier, F. Nüesch, C. Zhang, Turning trash into treasure: additive free MXene sediment inks for screen-printed micro-supercapacitors. *Adv. Mater.* (2020). <https://doi.org/10.1002/adma.202000716>
 41. N. Aslfattahi, L. Samylingam, A.S. Abdelrazik, A. Arifuzzaman, R. Saidur, MXene based new class of silicone oil nanofluids for the performance improvement of concentrated photovoltaic thermal collector. *Sol Energy Mater. Sol Cells* **211**, 110526 (2020). <https://doi.org/10.1016/j.solmat.2020.110526>
 42. O. Mashtalir, M. Naguib, V.N. Mochalin, Y. Dallgnese, M. Heon, M.W. Barsoum et al., Intercalation and delamination of layered

- carbides and carbonitrides. *Nat. Commun.* **4**, 1716 (2013). <https://doi.org/10.1038/ncomms2664>
43. M. Vural, A. Pena-Francesch, J. Bars-Pomes, H. Jung, H. Gudapati, C.B. Hatter et al., Inkjet printing of self-assembled 2D titanium carbide and protein electrodes for stimuli-responsive electromagnetic shielding. *Adv. Funct. Mater.* **28**, 1801972 (2018). <https://doi.org/10.1002/adfm.201801972>
 44. Y. Chae, S.J. Kim, S.Y. Cho, J. Choi, K. Maleski, B.J. Lee et al., An investigation into the factors governing the oxidation of two-dimensional Ti₃C₂ MXene. *Nanoscale* **11**, 8387–8393 (2019). <https://doi.org/10.1039/c9nr00084d>
 45. F. Rubbi, K. Habib, R. Saidur, N. Aslfattahi, S.M. Yahya, L. Das, Performance optimization of a hybrid PV/T solar system using Soybean oil/MXene nanofluids as A new class of heat transfer fluids. *Sol Energy* **208**, 124–138 (2020). <https://doi.org/10.1016/j.solener.2020.07.060>
 46. Q. Gao, M. Feng, E. Li, C. Liu, C. Shen, X. Liu, Mechanical, thermal, and rheological properties of Ti₃C₂Tx MXene/thermoplastic polyurethane nanocomposites. *Macromol. Mater. Eng.* **305**, 2000343 (2020). <https://doi.org/10.1002/mame.202000343>
 47. M. Greaves, S. Barg, M.A. Bissell, MXene-based anodes for metal-ion batteries. *Batter Supercaps.* **3**, 214–235 (2020). <https://doi.org/10.1002/batt.201900165>
 48. H. Tang, W. Li, L. Pan, C.P. Cullen, Y. Liu, A. Pakdel et al., In situ formed protective barrier enabled by sulfur@titanium carbide (MXene) ink for achieving high-capacity, long lifetime Li-S batteries. *Adv. Sci.* **5**, 1800502 (2018). <https://doi.org/10.1002/advs.201800502>
 49. C. Zhang, S.H. Park, A. Seral-Ascaso, S. Barwick, N. McEvoy, C.S. Boland et al., High capacity silicon anodes enabled by MXene viscous aqueous ink. *Nat. Commun.* **10**, 849 (2019). <https://doi.org/10.1038/s41467-019-08383-y>
 50. L. Yu, Z. Fan, Y. Shao, Z. Tian, J. Sun, Z. Liu, Versatile N-doped MXene ink for printed electrochemical energy storage application. *Adv. Energy Mater.* **9**, 1901839 (2019). <https://doi.org/10.1002/aenm.201901839>
 51. T. Gao, Z. Zhou, J. Yu, J. Zhao, G. Wang, D. Cao et al., 3D printing of tunable energy storage devices with both high areal and volumetric energy densities. *Adv. Energy Mater.* **9**, 1802578 (2019). <https://doi.org/10.1002/aenm.201802578>
 52. Z. Fan, C. Wei, L. Yu, Z. Xia, J. Cai, Z. Tian et al., 3D printing of porous nitrogen-doped Ti₃C₂ MXene scaffolds for high-performance sodium-ion hybrid capacitors. *ACS Nano* **14**, 867–876 (2020). <https://doi.org/10.1021/acsnano.9b08030>
 53. H. Li, X. Li, J. Liang, Y. Chen, Hydrous RuO₂ -decorated MXene coordinating with silver nanowire inks enabling fully printed micro-supercapacitors with extraordinary volumetric performance. *Adv. Energy Mater.* **9**, 1803987 (2019). <https://doi.org/10.1002/aenm.201803987>
 54. X. Li, H. Li, X. Fan, X. Shi, J. Liang, 3D-printed stretchable micro-supercapacitor with remarkable areal performance. *Adv. Energy Mater* **10**, 1903794 (2020). <https://doi.org/10.1002/aenm.201903794>
 55. S. Liu, X. Shi, X. Li, Y. Sun, J. Zhu, Q. Pei et al., A general gelation strategy for 1D nanowires: dynamically stable functional gels for 3D printing flexible electronics. *Nanoscale* **10**, 20096–20107 (2018). <https://doi.org/10.1039/c8nr06369a>
 56. M. Malaki, R.S. Varma, Mechanotribological aspects of MXene-reinforced nanocomposites. *Adv. Mater.* **32**, 2003154 (2020). <https://doi.org/10.1002/adma.202003154>
 57. S.A. Mirkhani, A. Shayesteh Zeraati, E. Aliabadian, M. Naguib, U. Sundararaj, High dielectric constant and low dielectric loss via poly(vinyl alcohol)/Ti₃C₂Tx MXene nanocomposites. *ACS Appl. Mater. Interfaces* **11**, 18599–18608 (2019). <https://doi.org/10.1021/acsami.9b00393>
 58. K. Hyun, M. Wilhelm, C.O. Klein, K.S. Cho, J.G. Nam, K.H. Ahn et al., A review of nonlinear oscillatory shear tests: analysis and application of large amplitude oscillatory shear (LAOS). *Prog. Polym. Sci.* **36**, 1697–1753 (2011). <https://doi.org/10.1016/j.progpolymsci.2011.02.002>
 59. H. Rastin, B. Zhang, A. Mazinani, K. Hassan, J. Bi, T.T. Tung et al., 3D bioprinting of cell-laden electroconductive MXene nanocomposite bioinks. *Nanoscale* **12**, 16069–16080 (2020). <https://doi.org/10.1039/D0NR02581J>
 60. W.L. Zhang, W. Wei, W. Liu, T. Guan, Y. Tian, H. Zeng, Engineering the morphology of TiO₂/carbon hybrids via oxidized Ti₃C₂Tx MXene and associated electrorheological activities. *Chem. Eng. J.* **378**, 122170 (2019). <https://doi.org/10.1016/j.cej.2019.122170>
 61. W.L. Zhang, J. Tian, H. Zeng, J. Liu, Y. Tian, Promoted electro-responsive performances in an interface-confined oxidized niobium carbide MXene. *Chem. Eng. J.* **366**, 321–329 (2019). <https://doi.org/10.1016/j.cej.2019.02.065>
 62. M.A. Hope, A.C. Forse, K.J. Griffith, M.R. Lukatskaya, M. Ghidiu, Y. Gogotsi et al., NMR reveals the surface functionalisation of Ti₃C₂ MXene. *Phys. Chem. Chem. Phys.* **18**, 5099–5102 (2016). <https://doi.org/10.1039/c6cp00330c>
 63. V. Natu, M. Benchakar, C. Canaff, A. Habrioux, S. Célérier, M.W. Barsoum, A critical analysis of the X-ray photoelectron spectra of Ti₃C₂Tz MXenes. *Matter* **4**, 1224–1251 (2021). <https://doi.org/10.1016/j.matt.2021.01.015>
 64. L.H. Karlsson, J. Birch, J. Halim, M.W. Barsoum, P.O.Å. Persson, Atomically resolved structural and chemical investigation of single MXene sheets. *Nano Lett.* **15**, 4955–4960 (2015). <https://doi.org/10.1021/acs.nanolett.5b00737>
 65. C.J. Zhang, S. Pinilla, N. McEvoy, C.P. Cullen, B. Anasori, E. Long et al., Oxidation stability of colloidal two-dimensional titanium carbides (MXenes). *Chem Mater* **29**, 4848–4856 (2017). <https://doi.org/10.1021/acs.chemmater.7b00745>
 66. R. Ibragimova, M.J. Puska, H.P. Komsa, pH-dependent distribution of functional groups on titanium-based MXenes. *ACS Nano* **13**, 9171–9181 (2019). <https://doi.org/10.1021/acsnano.9b03511>

67. S. Naficy, R. Jalili, S.H. Aboutalebi, R.A. Gorkin III., K. Konstantinov, P.C. Innis et al., Graphene oxide dispersions: tuning rheology to enable fabrication. *Mater. Horiz.* **1**, 326–331 (2014). <https://doi.org/10.1039/C3MH00144J>
68. G. Siqueira, D. Kokkinis, R. Libanori, M.K. Hausmann, A.S. Gladman, A. Neels et al., Cellulose nanocrystal inks for 3D printing of textured cellular architectures. *Adv. Funct. Mater.* **27**, 1604619 (2017). <https://doi.org/10.1002/adfm.201604619>